nature communications

Article

https://doi.org/10.1038/s41467-026-70655-1

Mutant ribosomal protein RPS15 drives B cell malignancy through oxidative stress and genomic instability

Received: 6 February 2024

Accepted: 2 March 2026

Published online: 30 March 2026

Check for updates

Catherine Gutierrez[1,2,18], Marwan Kwok[1,2,3,4,5,18], Neil Ruthen[2,18], Peyton Waddicor[1,2], Christina Curran[2,6], Tamara Ouspenskaia[3], Doris Fu[3,7], Brendan Smalec[1], Samantha Sedor[1], Binyamin A. Knisbacher[3,8], Anat Biran[2], Adi Nagler[2], Filip Garbicz[2,9], Tomasz Sewastianik[2], Johany Penailillo[2], Fabienne Lucas[9], Shanye Yin[2], Aviv Liani[2,6], Sarah Chen[3], Gregory Lazarian[2,10,11], Elizabeth Witten[2], Nathan Dangle[2], Ella L. Brunsting[2], Mei Zheng[9], Emma S. Lin[2], Madison J. Lee[2,6], Blake Wells[1], Lucas Pomerance[1,2], María Hernández-Sánchez[12], Shuqiang Li[2,3,13], Ziao Lin[1,3], Aziz Al'Khafaji[3], Lili Wang[14], Sudhir Thakurela[2], Kenneth J. Livak[3,13], Donna Neuberg[15], Florence Cymbalista[10,11], Gad Getz[1,3,16,17], Aviv Regev[3], Stirling Churchman[1], Elisa ten Hacken[1,2], Ruben Carrasco[1,2,9], Sichen Shao[1] & Catherine J. Wu[1,2,3] ✉

Ribosomal protein mutations are increasingly associated with cancer risk and thought to perturb ribosome function. At the same time, they reportedly activate p53, a critical anti-cancer barrier. To determine how these mutations overcome this protective block to enable tumorigenesis, we generate an in vivo model of the hotspot ribosomal protein *RPS15*-S138F mutation identified as a putative driver of chronic lymphocytic leukemia. Under pre-leukemic conditions, this mutation induces ribosome biogenesis defects and altered translation resulting in oxidative stress, DNA damage and induction of a p53-dependent response that promote initial cellular hypo-proliferation. However, a subset of aged mice with mutated *Rps15* eventually develop B-cell leukemia (37% penetrance), which exhibits increased Myc activity with strong pro-survival and proliferation signatures. Mutant *RPS15* thus induces both hypo- and hyper-proliferative signals, initially weighted towards cell cycle arrest; and that through translational rewiring, oxidative stress, DNA damage response defects and genomic instability set the stage for the acquisition of additional driving mutations, such as *TP53* deletion, that can overcome this cell cycle block to trigger tumorigenesis.

Mutations in ribosomal proteins resulting in ribosomopathies are associated with an increased risk for cancer in humans[1]. Recent large-scale cancer sequencing studies have identified ribosomal protein mutations across solid and hematologic malignancies, further implicating them as possible cancer drivers[2–7]. In chronic lymphocytic leukemia (CLL), recurrent hotspot mutations have been identified in the ribosomal protein gene *RPS15* (~5% of untreated patients)[8,9]. These mutations are often clonal[8] and are further enriched (~20%) in relapsed

A full list of affiliations appears at the end of the paper. ✉e-mail: catherine_wu@dfci.harvard.edu

CLL following chemoimmunotherapy[10] and targeted therapy[11], suggesting a yet unproven role in early transformation and disease progression. Collectively, these observations have fueled growing interest in the mechanisms by which altered ribosomal proteins may promote oncogenesis.

The human ribosome, comprised of ~6000 ribosomal RNA (rRNA) bases and 80 ribosomal proteins assembled into small (40S) and large (60S) subunits, is constructed in a complex and energetically costly process within both the nucleus and cytoplasm[12]. The ribosome assembly process begins in the nucleolus with the transcription and modification of rRNA followed by export of pre-40S and pre-60S particles to the cytoplasm for assembly of mature 40S and 60S subunits into 80S ribosomes. Accumulating evidence suggests that ribosome heterogeneity, including diversity in ribosomal proteins, ribosomal mutations, and ribosomal RNA allele usage and modifications can impact ribosome function and protein translation, thereby contributing to cellular rewiring that ultimately promotes tumor progression[13–18]. On the other hand, changes in ribosomal protein expression or function often have deleterious impact on the cell[19,20]. Accordingly, they activate tumor suppressors (e.g., *TP53*) that respond to alterations in ribosome function by inhibiting ribosome production, rRNA synthesis and cell cycling, hence promoting cellular quiescence[21–23]. Indeed, several ribosomal proteins, including RPS15, directly interact with MDM2, which ubiquitinates p53 and thus modulates its activity[24–30]. In ribosomopathies, this characteristic transition from a hypo-proliferative to a hyper-proliferative state with elevated cancer risk is a well-recognized paradox, so-called 'Dameshek's riddle' [31,32].

Multiple previous studies have sought to address the mechanisms underlying such paradoxical transitions in the context of different ribosomopathies, as well as their link with oncogenic predisposition and tumor development. Focusing on modeling of the *RPL10*-R98S T-ALL mutation in Ba/F3 cells and in patient-derived xenotransplantation models, a previous study demonstrated that the accumulation of oxidative stress in *RPL10*-R98S cells resulted in their impaired proliferation, with BCL-2 overexpression in these cells allowing them to tolerate high oxidative stress levels[16]. In a further study, patients with T-ALL harboring *RPL10*-R98S and other ribosomal gene mutations were shown to display increased mutation burden, an enrichment of *NOTCH1* mutations, and a mutation signature characterized by C:G>A:T transversions[18]. Further modeling on Ba/F3 and murine lymphoid cells demonstrated mitigation of *RPL10* R98S-associated oxidative stress and cellular hypo-proliferation by *NOTCH1* mutation[8,16–18]. Elevated oxidative stress levels associated with ribosomal gene mutations have also been reported in lymphoid cells from patients with Diamond-Blackfan anemia[33]. In the context of *RPS15* mutations in CLL, translational alterations with resultant changes in the global cellular proteome have been demonstrated within in vitro models[10,34,35]. Additionally, reanalysis by Sulima et al. of our previously published genomics dataset from the German CLL Study Group (GCLL)-CLL8 trial showed higher mutation burden across CLL tumors harboring ribosomal gene alterations, reminiscent of findings in T-ALL[8,18]. However, no in vivo animal model of *RPS15*-mutant CLL has thus far been developed, and the role of *RPS15* defects as an oncogenic driver remains hitherto unproven. Moreover, the in vivo phenotypic and functional consequences of *RPS15* mutations in CLL are unknown, and the association between oxidative stress and translational defects has not been definitively established.

To determine whether *RPS15* mutation can drive B-cell oncogenesis, either singularly or in combination, and to define the mechanisms by which it might do so, we engineered a mouse model recapitulating a representative hotspot *RPS15* mutation, *RPS15*-S138F. We demonstrate that *Rps15*-S138F leads to CLL development in elderly mice, with earlier onset and more aggressive disease when co-mutated with *Trp53*. We also uncover an array of translational defects induced by *RPS15* mutations and delineate the mechanisms by which these defects drive tumor progression. Collectively, our results reveal, in vivo, how *RPS15* mutations pivot cells from an initial hypo-proliferative pre-malignant phase to a subsequent hyper-proliferative malignant state and support a mechanistic model by which *RPS15* mutation generates "oncogenic ribosomes".

Results

RPS15 mutation co-occurs with TP53 mutation in CLL and is associated with poorer OS

To evaluate the co-occurrence of *RPS15* mutation (*mut-RPS15*) with other common CLL drivers, we identified CLL samples bearing mut-*RPS15* from two independent cohorts. One was the 'CLL-map'[36], in which 26 of 1,063 CLL specimens, profiled by either whole-exome or whole-genome sequencing (WES, WGS), were identified as bearing mut-*RPS15* (allelic frequency [AF] >3%; Supp Data 1). The other was the "French cohort", wherein 19 of 277 prospectively collected independent CLL samples characterized by targeted next-generation sequencing of a panel of putative CLL drivers (e.g., *RPS15*, *NOTCH1*, *FBXW7*, *POT1*, Methods) were identified as harboring mut-*RPS15* (AF > 1%) (Fig. 1a, Supp Fig. 1a, Supp Table 1). *RPS15* mutations from both patient cohorts occurred exclusively within exon 4 in a region spanning amino acids 129-145 in the C-terminal region of the protein (Fig. 1b). This localized pattern was consistent with previous data, and mutations in this region have been shown to have effects on ribosome assembly and maturation in yeast[37], as well as on translation in HEK293T[34] and primary CLL cells[35]. Twenty-two *RPS15* mutations from these 45 (49%) cases across the two cohorts were clonal (AF > 35%), suggesting a possible role for mut-*RPS15* in early CLL development. These cases almost uniformly (43 of 45 [96%]) displayed unmutated *IGHV* status ('U-CLL').

Of the U-CLL cases, as has been also reported by others[8,10,38], the most common co-occurring mutation was alteration in *TP53* (Supp Fig. 1b), either as deletion in chromosome 17 (*del*[17p]), *TP53* mutation, or both (in 13 of 43 [30.2%], compared to 16.4% of U-CLL without *mut-RPS15*, OR = 2, $p = 0.075$). *RPS15*-mutated samples also harbored mutations in other genes associated with DNA damage response and maintenance of genome stability (i.e., *ATM*, *POT1* and *DDX3X*)[39], though none of these associations were statistically significant. The CLL-map cohort further provided an opportunity to evaluate how *RPS15* mutation might link with a broader array of alterations beyond a limited targeted panel. *Mut-RPS15* (located on human chromosome 19) was associated with copy number alterations (CNAs) in chromosome 6q, including arm-level *del*(6q) ($n = 6$) and focal *del*(6q25.3) ($n = 7$) (Supp Fig. 1b), as compared to wild-type *RPS15* U-CLL cases (50% vs 16% [74 of 463], OR 5.2, $p = 0.0001$). Arm-level *del*(6q) has been previously detected in CLL and is associated with adverse prognosis in diverse lymphoid malignancies[40]. The deleted region of *del*(6q25.3) encodes *EZR* (a known oncogene in solid tumors, reported to play a role in the activation of BCR-mediated signaling in B-cell lymphomas)[41,42], *C6orf99* (an autophagy-related long non-coding RNA associated with breast cancer survival)[43], *OSTCP1* (a transmembrane glycoprotein that constitutes a key hub of oncogenic signaling and associated with progressive disease and poor survival)[44], and *MIR3918* (a BCL2 inhibitor implicated in numerous cancers) [45,46].

RPS15 mutations in CLL have previously been associated with inferior prognosis[8,10]. In our dataset, where we stratified samples by *IGHV* mutation status, U-CLLs with either sole *RPS15* mutation, sole *TP53* alteration, and both *RPS15* mutation and *TP53* alteration (including *TP53* mutation, *del*(17p) and *del*(17p13.1)) did not have a difference in OS, but altogether had shorter overall survival (OS) compared to cases without *RPS15* or *TP53* mutation ($p = 0.0045$, comparison of all four groups, log-rank test, Supp Fig. 1c). U-CLLs with wildtype *TP53* and *RPS15* mutations only trended to a shorter overall survival (OS) compared to cases with wild-type *RPS15* ($p = 0.096$) but did not reach statistical significance.

https://doi.org/10.1038/s41467-026-70655-1

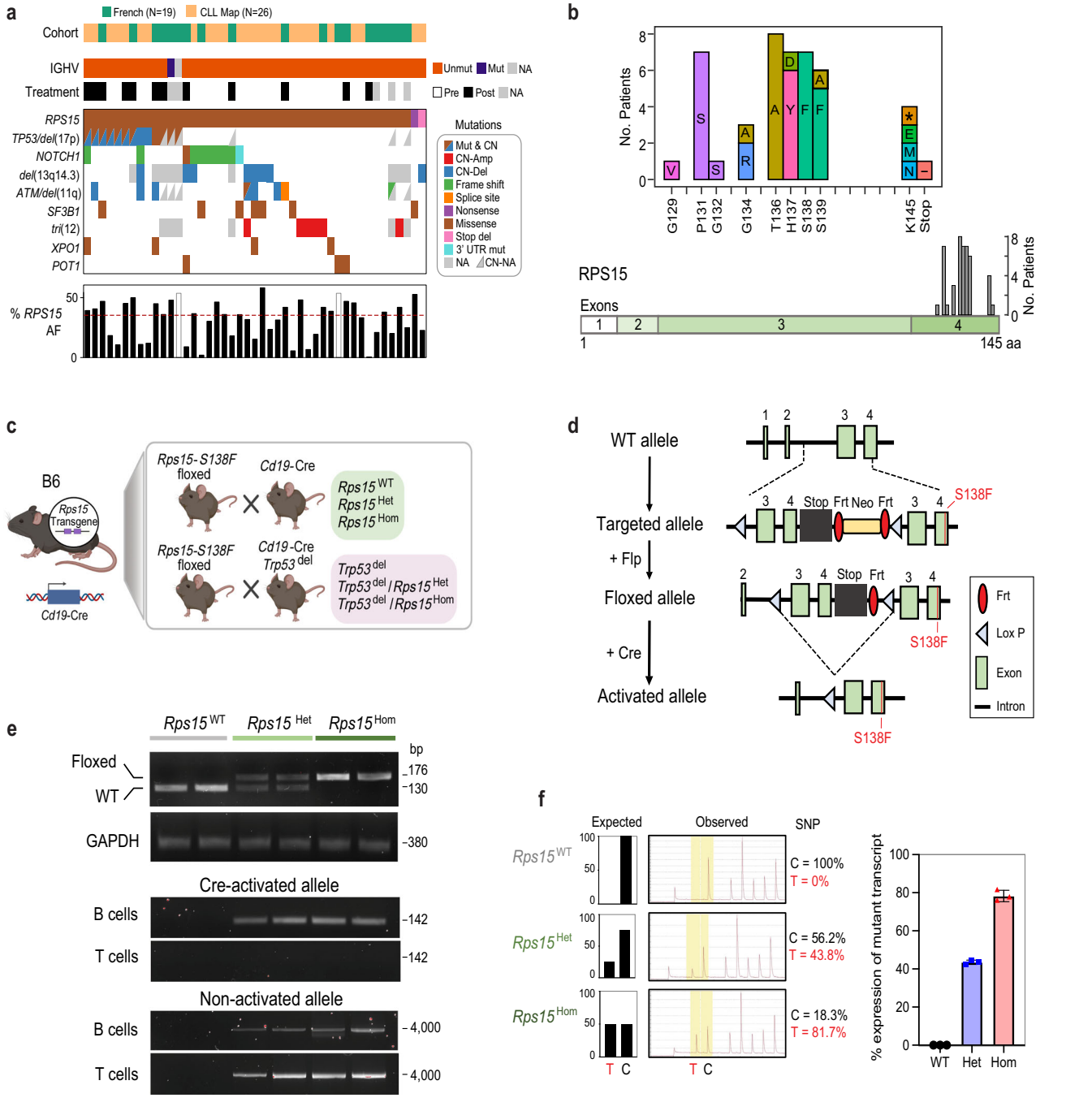

Fig. 1 | *RPS15* is recurrently mutated in CLL in a hot-spot region that impacts the mRNA/ribosome interaction. a Co-mutation plot of WES and targeted NGS data demonstrating co-occurrence of *RPS15* and other known CLL driver mutations across *RPS15*-mutated patient CLL samples (CLL Map and French cohorts). Mut=-mutation (SNV or InDel); CN=Copy Number alterations. NA=data not available. Bottom panel: Mutations were designated as clonal mutations if their percent allelic frequencies (% *RPS15* AF, black bars) exceeded a threshold of 35% (red dashed line); white bars- % RPS15 AF undetermined). **b** Exon localization of *RPS15* mutations identified in patient CLL samples. '*'=stop codon; '-'=end of the gene; aa=amino acids. **c** Schematic of single and double-mutant mouse cohorts, generated by the intercrossing of mouse strains generated using the gene-editing approach shown in **d**. Created in BioRender. Gutierrez, C. (2025) https://BioRender.com/8kf56if. **d**, Schematic of the gene editing approach for the Cre/Flox *Rps15*-S138F B6 (Black 6) mouse model. The targeted allele is activated following exposure to the recombinase flippase (Flp) and subsequently, to Cre recombinase (Cre) (see Methods). **e** *Rps15*-S138F allele activation was restricted to B cell DNA as ascertained by DNA PCR. **f**, Percentage of WT and mutant *Rps15* alleles from targeted RNA sequencing. Left: representative pyrosequencing traces from 1 mouse per genotype. Right: quantified profiles from $n = 3$ mice per genotype. Data in the bar plots are presented as mean values ± standard deviation (SD).

Rps15-S138F mutation drives B-cell transformation in vivo

To directly interrogate the effects of *RPS15* mutation on B-cell function, we engineered a mouse model with conditional expression of *Rps15-S138F*, which is among the most commonly occurring of *RPS15* mutations, using the *Cd19*-Cre/*loxP* system (Fig. 1c, Supp Fig. 1d, Methods). By intercrossing *Cd19*-Cre and *Rps15*-loxP mice (Fig. 1d), we generated cohorts of wild-type (WT) (*Cd19*-Cre/*Rps15*$^{+/+}$, '*Rps15*^{WT}'), heterozygous (*Cd19*-Cre/*Rps15*$^{fl/+}$, '*Rps15*^{Het}' or Het), and homozygous (*Cd19*-Cre/*Rps15*$^{fl/fl}$, '*Rps15*^{Hom}' or Hom) mutant (MT) mice. Further, as *TP53* heterozygous deletions often co-occur with *RPS15* mutation, we intercrossed *Cd19*-Cre/*Rps15*^{MT} mice with *Trp53* heterozygously-deleted mice (*Trp53*^{del}) to generate *Trp53*^{del}/*Rps15*^{MT}

co-mutant murine cohorts (Methods). Targeted PCR confirmed the presence of the floxed allele and Cre-mediated activation of the mutant allele exclusively in CD19$^+$ splenic B cells (Fig. 1e). Moreover, we confirmed stable expression of the mutant *Rps15* allele by quantitative targeted RNA sequencing of splenocytes (Fig. 1f) from both heterozygous (~50% of transcripts) and homozygous (~80% of transcripts) young mice (3-6 months of age) and was expressed at similar levels in older mice (>12 months of age) (Supp Fig. 1e). We noted no significant differences in RPS15 protein levels across genotypes in young pre-leukemic mice (Supp Fig. 1f).

To determine whether *Rps15* mutation alone is sufficient to drive B-cell leukemogenesis, we monitored the peripheral blood of three cohorts of mice (*Rps15*^{WT}, *Rps15*^{Het}, *Rps15*^{Hom}, $n = 30$ each) bi-monthly via flow cytometry for the appearance of B220$^+$CD5$^+$ CLL-like cells for up to 24 months of age (gating strategy in Supp Fig. 2a-b). No circulating CLL-like cells were detected in any *Rps15*^{WT} mice, yet 11 of 30 (37%) *Rps15*^{Het} mice and 3 of 30 (10%) *Rps15*^{Hom} mice developed CLL-like disease between the ages of 18-24 months ($p = 0.03$; Fig. 2a-b), confirmed by CD5/PAX5 immunohistochemical staining of tissue sections (Fig. 2c, Supp Fig. 2c).

Given the frequent co-occurrence of *TP53* heterozygous deletion in *RPS15*-mutant CLL, we also monitored three additional cohorts of mice with heterozygous *Trp53 deletion* (*Rps15*^{WT}/*Trp53*^{del} [hereafter *Trp53*^{del}], *Rps15*^{Het}/*Trp53*^{del} and *Rps15*^{Hom}/*Trp53*^{del} [hereafter combined, *Rps15*^{MT}/*Trp53*^{del}], $n = 30$ each). As expected, given that *TP53* is a known CLL driver, we observed circulating CLL-like disease in 7 of 30 (23%) *Trp53*^{del} mice (Fig. 2a). Unlike the single-mutant cohort, where heterozygous *Rps15* mutant mice predominantly developed B-cell leukemia reminiscent of human CLL, this was seen in only 3 of 30 (10%) *Trp53*^{del}/*Rps15*^{Het} mice; instead, 8 of 30 (27%) *Trp53*^{del}/*Rps15*^{Hom} developed CLL-like disease ($p = 0.18$).

We additionally observed four cases of diffuse large B-cell lymphoma (DLBCL) unique to the *Rps15*^{MT}/*Trp53*^{del} cohorts, as determined by massive splenomegaly (Fig. 2d) and characteristic histological and immunohistochemical features, including the presence of large B cells that formed confluent sheaths, MYC/IRF4 positivity, BCL6 negativity and high Ki-67 proliferation index (Supp Fig. 2c-e). This finding is of particular relevance given growing reports of *RPS15* mutations (including S138F) identified in human Richter's Syndrome (RS) characterized by high-grade transformation of CLL to DLBCL[47–49], and stands in stark contrast to prior assumptions that *RPS15* is a passenger mutation present in *TP53*-mutant cells, rather than an independent driver of RS. In all cases, mice with CLL or DLBCL-like disease, whether arising from Rps15-mutant mice (both *Rps^{Het}* and *Rps^{Hom}*) or from compound mutant mice (with *Trp53^{del}*), exhibited extensive tumor infiltration of the spleen and peritoneal cavity. For CLL mice, bone marrow involvement was minimal, but was greater for RS/DLBCL mice (Supp Fig. 2f).

Consistent with our patient data, next-generation sequencing analysis of BCRs revealed that all murine CLL-like tumors harbored unmutated IGHV (Supp Data 2). Furthermore, we identified increased marginal zone B cells (B220$^+$ CD21^{high} CD23$^-$) in *Rps15*^{Hom} mice compared to *Rps15*^{WT} mice ($p = 0.005$; Supp Fig. 3a–c) with relative reduction of follicular B cells (B220 + CD21- CD23^{high,} $p = 0.05$) and B1a cells (B220$^+$ CD5^{high}, $p < 0.0001$) and no change in B1b (B220$^+$ CD5^{low}) or transitional B cells (Supp Fig. 3c, d). These data indicate that the CLL-like disease likely emerged from marginal zone B cells rather than follicular, B1a, B1b or transitional B cells.

Transcriptional profiling of leukemic and pre-leukemic Rps15-mutant B cells reveals distinct hyper-proliferative and hypo-proliferative signatures

To elucidate the molecular events contributing to *Rps15*-mutant leukemogenesis, we performed transcriptome analysis of CLL-like (B220 + CD5 +) cells isolated through fluorescence-activated cell sorting (FACS) of splenocytes from *Rps15*^{Het} mice ($n = 3$) and from normal B cells obtained from spleens of age-matched *Rps15*^{WT} mice ($n = 3$) (all 24 months of age). Principal component (Supp Fig. 3e) and differential gene expression analysis (Fig. 2e-left, Supp Table 2) revealed clear differences in gene expression between CLL-like and non-CLL B cells, with 2106 upregulated and 1972 downregulated genes in CLL-like cells ($\log_2FC > 0.3$, $q < 0.05$). Gene set enrichment analysis (GSEA) revealed marked upregulation of the Myc transcriptional program in *Rps15*^{Het} CLL-like cells (Fig. 2e-right), as well as upregulation of cell cycle, DNA repair, and B cell receptor signaling programs (Supp Fig. 3f). Upregulation of Myc target genes could also be recapitulated in *RPS15*-S138F mutant vs WT isogenic HG3 cell lines with and without *TP53* knockout, and in primary samples from 3 treatment-naïve CLL patients harboring clonal *RPS15* mutations, compared to 3 *RPS15* WT CLL samples of similar genetic background (Fig. 2f, Supp Fig. 3g). Reactome pathway analysis of these differentially expressed signatures across all three contexts (i.e., murine and cell line models, and primary CLL samples) revealed a common enrichment in translational machinery, such as mRNA splicing and processing, rRNA processing and modification, snRNP assembly, and N-glycosylation of protein (Supp Fig. 3h, normalized enrichment score>1, nominal p-value < 0.05).

To determine whether similar transcriptional signatures could be observed in the setting of pre-leukemia, we performed RNA sequencing (RNA-seq) analysis of splenic B cells from 3 to 6-month-old *Rps15*^{WT}, *Rps15*^{Het}, and *Rps15*^{Hom} mice ($n = 3$ per genotype). We identified a total of 59 and 432 significantly upregulated and 192 and 325 significantly downregulated genes in *Rps15*^{Het} vs *Rps15*^{WT} mice and *Rps15*^{Hom} vs *Rps15*^{WT} mice, respectively (Fig. 3a, Supp Data 3; $\log_2FC > 0.3$, $q < 0.05$). While GSEA of differentially expressed genes in *Rps15*^{Het} vs *Rps15*^{WT} B cells from 3-6 month old mice exhibited downregulation of Myc target genes (Supp Fig. 4a, Supp Data 4), these genes were found to be upregulated in *Rps15*^{Het} vs *Rps15*^{WT} non-CLL B cells in aged mice (24 month old) (Supp Fig. 4b, c, Supp Table 2, Supp Data 5). Comparison of *Rps15*^{Hom} vs *Rps15*^{WT} pre-leukemic B cells (3-month-old) also revealed a marked enrichment of Myc target genes (Fig. 3b), similar to *Rps15*^{Het} CLL-like tumor cells (Fig. 2e, f). Concomitantly, B cells from 3 to 6-month-old pre-leukemic *Rps15*^{Het} and *Rps15*^{Hom} mice displayed downregulation of genes involved in DNA replication, cell cycle regulation, mitosis, DNA repair as well as cellular metabolism and turnover (Fig. 3b, Supp Fig. 4a). The latter suggests that proportionately fewer *Rps15*^{Het} and *Rps15*^{Hom} pre-leukemic B cells were actively cycling compared to their *Rps15*^{WT} counterpart. Consistent with this finding, we observed a reduced proportion of B cells in the peripheral blood of aged pre-leukemic *Rps15*^{Hom} vs *Rps15*^{WT} mice ($p < 0.0001$, Fig. 3c), accompanied by lower ex vivo proliferative capacity in both *Rps15*^{Het} and *Rps15*^{Hom} B cells compared to *Rps15*^{WT} B cells upon mitogenic stimulation with lipopolysaccharide (LPS) ($p = 0.0007$, Fig. 3d, Supp Fig. 4d). Thus, while *Rps15*-mutant CLL cells displayed exclusively hyper-proliferative transcriptional signatures, hypo-proliferative signatures co-existed with and predominated over hyper-proliferative signatures in pre-leukemic *Rps15*-mutant B cells.

Rps15-mutant pre-leukemic B cells accumulate oxidative stress and DNA damage

To reconcile the paradoxical finding of B-cell hypo-proliferation in 3–6-month-old *Rps15*-mutant mice with their leukemic potential, we focused our functional analysis on splenic B cells from these pre-leukemic mice. Informed by the downregulation of cell cycle genes from our RNA-seq analysis (Fig. 3b; Supp Fig. 4a), we performed cell cycle profiling, which showed increased G1 cell cycle checkpoint activity in pre-leukemic *Rps15*^{Het} and *Rps15*^{Hom} versus *Rps15*^{WT} B splenocytes, particularly at 24 hours following induction of proliferation ($p = 0.003$ and $p = 0.013$, respectively, Fig. 3e, Supp Fig. 4e). In *Rps15*^{Hom} B cells, we additionally observed increased early and late apoptotic activity compared to *Rps15*^{WT} cells ($p = 0.0002$ and $p = 0.02$, respectively 48 h following LPS treatment, Fig. 3f).

https://doi.org/10.1038/s41467-026-70655-1

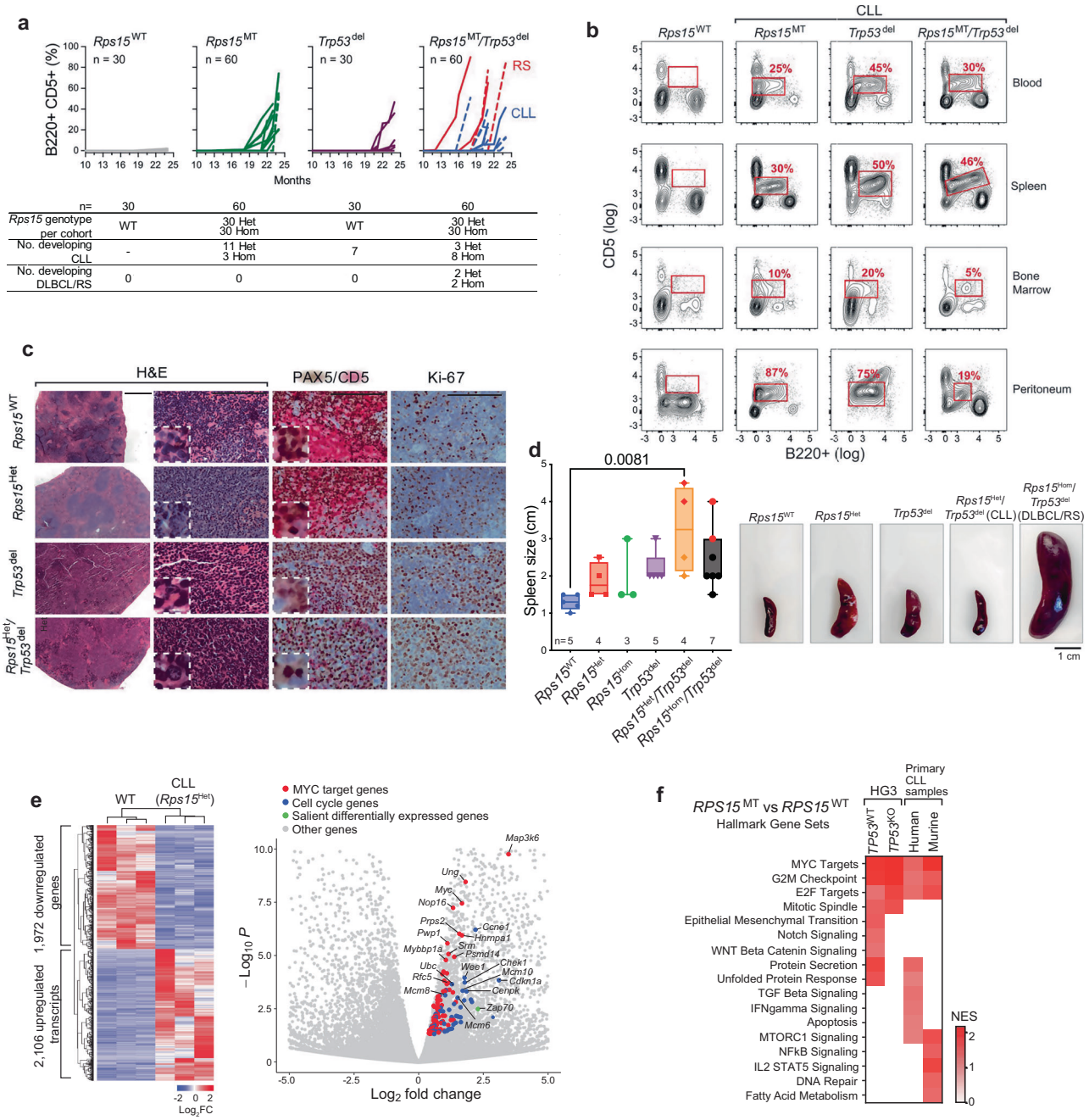

n=	30	60	30	60
Rps15 genotype per cohort	WT	30 Het 30 Hom	WT	30 Het 30 Hom
No. developing CLL	-	11 Het 3 Hom	7	3 Het 8 Hom
No. developing DLBCL/RS	0	0	0	2 Het 2 Hom

Fig. 2 | *Rps15*-S138F mutation drives CLL and DLBCL development in aged mice. **a** Top: B220 + CD5+ cells in peripheral blood (flow cytometry gating strategy: Supp Fig. 2a) over time in Rps15^{WT}, *Rps15*^{MT} (*Rps15*^{Het}, *Rps15*^{Hom}), *Trp53*^{del} and double mutant mice cohorts. Solid lines=*Rps15*^{Het}; Dotted lines=*Rps15*^{Hom}. Bottom: number of cases of CLL and DLBCL/RS per group, with breakdown of cases arising from *Rps15*^{Het} vs *Rps15*^{Hom} mice. **b** B220 + CD5+ cells within peripheral blood, spleen, bone marrow and peritoneum of *Rps15*^{WT}, *Rps15*^{Het}, *Trp53*^{del} and *Rps15*^{Het}/*Trp53*^{del} CLL mice (flow cytometry gating strategy: Supp Fig. 2a). Data for *Rps15*^{Hom} mice not shown due to lack of available tissue. Data shown are representative of 30 *Rps15*^{WT}, 11 *Rps15*^{Het}, 7 *Trp53*^{del} and 3 *Rps15*^{Het}/*Trp53*^{del} CLL mice. **c**, H&E staining and IHC staining of CD5 + PAX5+ and Ki-67+ cells in splenic tissue (black scale bar = 0.25 mm). Data shown are representative of 5 *Rps15*^{WT}, 4 *Rps15*^{Het}, 5 *Trp53*^{del} and 4 *Rps15*^{Het}/*Trp53*^{del} CLL mice. CD5, MYC, PAX5, BCL6 and IRF4 IHC staining is provided in Supp Fig. 2c, d. **d** Left: spleen size from mice across cohorts. Animals evaluated per genotype: *Rps15*^{WT} $n = 5$; *Rps15*^{Het} $n = 4$; *Rps15*^{Hom} $n = 3$; *Trp53*^{del} $n = 5$; *Rps15*^{Hom}/*Trp53*^{del} n = 4; *Rps15*^{Hom}/*Trp53*^{del} $n = 7$. Red symbols denote RS animals. Statistical analysis was performed using ANOVA with Tukey multiple comparisons tests (two-sided). Right: representative spleens from indicated genotypes. Median values indicated by horizontal lines. Bar = 1 cm. Box bounds represent the 25th and 75th percentile (interquartile range [IQR]); 50th percentile (median) and outliers are shown. **e** Left: Heatmap showing normalized expression of top dysregulated genes in CLL cells from *Rps15*^{Het} mice vs normal B cells from *Rps15*^{WT} mice (3 mice per condition, 24 months of age). Right: Volcano plot of differentially expressed genes in CLL (from *Rps15*^{Het} mice) vs normal B cells and two upregulated gene-sets from the former (log2FC > 0.3, DESeq2 FDR-adjusted two-sided Wald test $p < 0.05$, GSEA FDR-adjusted two-sided empirical $p < 0.25$); see Supp Table 2, Supp Data 5 for affected pathways. **f** GSEA analysis (Hallmark) reveals top differentially expressed pathways across *RPS15*-mutant (±*TP53* KO) HG3 cell lines, murine (*Rps15*^{Het}) and primary human (*RPS15*-mut) CLL samples compared to their *Rps15*/*RPS15*-WT counterpart (NES > 1, GSEA FDR-adjusted two-sided empirical $p < 0.05$). Additional data are provided in Supp Fig. 3.

https://doi.org/10.1038/s41467-026-70655-1

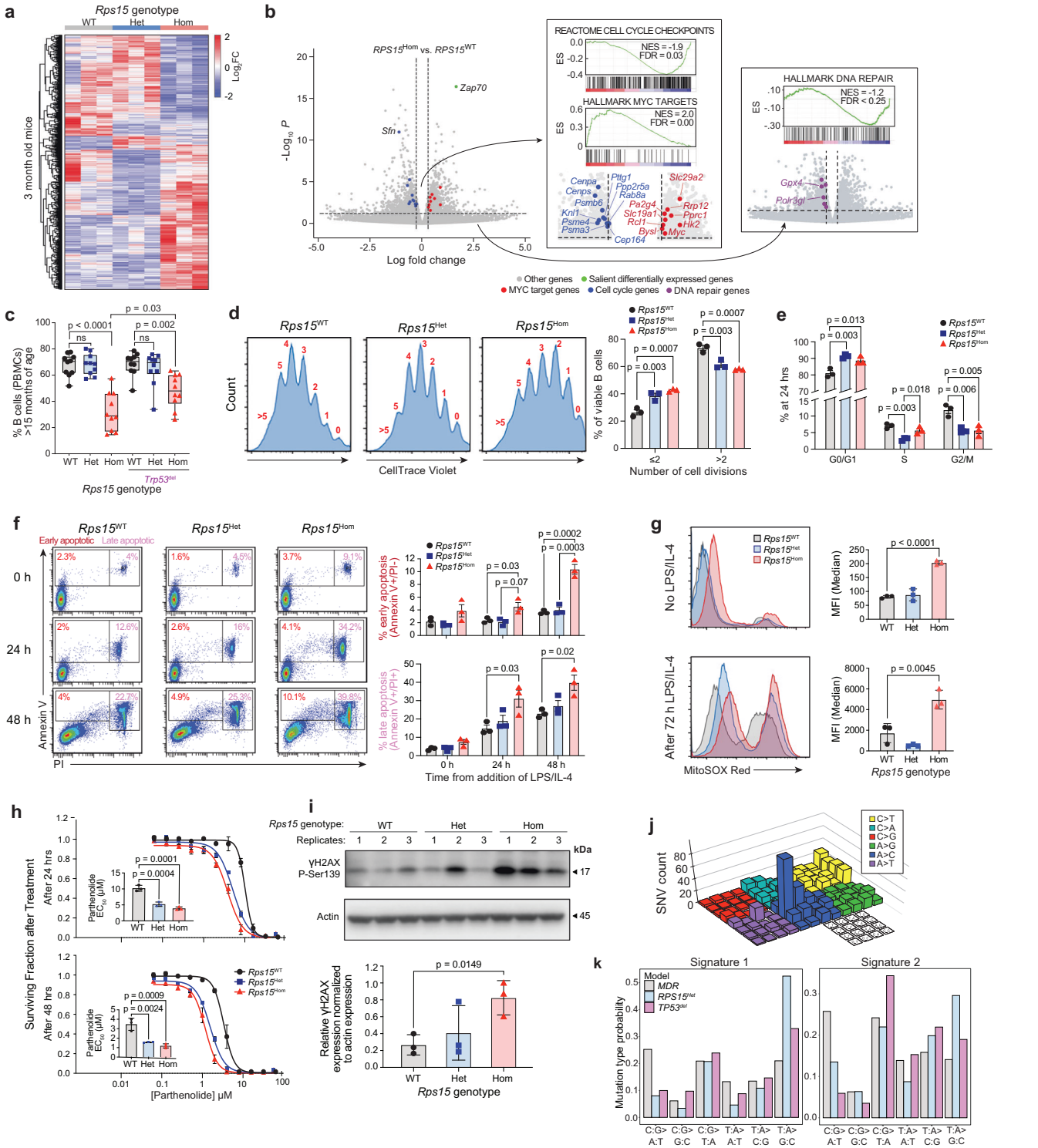

We hypothesized that the suppression of proliferation and potentiation of apoptosis in pre-leukemic *Rps15*^{Hom} B cells despite Myc upregulation could arise from increased cellular stress in these cells resulting from *Rps15* mutation. Consistent with the notion that enhanced oxidative stress is present in *Rps15*^{Hom} compared *Rps15*^{WT} B cells, transcriptomic analysis revealed a marked increase in expression of reactive oxygen species (ROS) genes in B splenocytes from pre-leukemic *Rps15*^{Hom} compared to *Rps15*^{WT} mice (NES 1.5, GSEA FDR-adjusted two-sided empirical $p < 0.05$) (Supp Data 4). Further, functional evidence of increased oxidative stress in both quiescent and proliferating *Rps15*^{Hom} B splenocytes ($p < 0.0001$ and $p = 0.0045$ respectively compared to *Rps15*^{WT}), as well as in quiescent *Rps15*^{Het} B splenocytes from older (11 month old) pre-leukemic mice ($p = 0.026$ compared to *Rps15*^{WT}), was confirmed by experimental quantification of mitochondrial ROS (Fig. 3g; Supp Fig. 4f; Supp Fig. 4g). Accordingly, *Rps15*^{Hom} B cells exhibited hypersensitivity to further potentiation of oxidative stress with parthenolide (EC_{50} 3.5 μM vs 1.2 μM for *Rps15*^{Hom} vs *Rps15*^{WT} with 48 h of treatment, $p = 0.0009$, Fig. 3h), a compound selected specifically for its known potent pro-oxidant effect on CLL cells [50–52].

We reasoned that elevated oxidative stress in *Rps15*-mutant B cells, if unresolved, could lead to deleterious accumulation of DNA damage. Accordingly, we observed an increased accumulation of

Fig. 3 | *Rps15* mutations confer a distinct B cell phenotype characterized by decreased proliferation and increased apoptosis associated with increased oxidative stress and DNA damage accumulation. a Heatmap showing normalized expression of top dysregulated genes in B cells from *Rps15*^{WT}, *Rps15*^{Het} and *Rps15*^{Hom} mice ($n = 3$ per genotype, 3 months old). **b** Volcano plot of differentially expressed genes in pre-leukemic *Rps15*^{Hom} vs *Rps15*^{WT} murine B cells (3–6 months old) highlighting notable gene-sets using GSEA (log2FC > 0.3, DESeq2 two-sided Wald test p < 0.05, GSEA FDR-adjusted two-sided empirical $p < 0.25$). ES=enrichment score. NES=Normalized enrichment score. **c**, Proportion of B cells relative to total lymphocytes in peripheral blood of *Rps15*^{WT}, *Rps15*^{Het} and *Rps15*^{Hom} mice ($n = 10$ per genotype, >15 months old), with and without *Trp53* heterozygous deletion. Gating strategy: Supp Fig. 2a. Minima/minima, IQR, and 50th percentile are shown. **d** Proliferative potential of murine B cells 72 hours after ex vivo mitogenic stimulation with LPS/IL-4. Histogram peaks shows the number of cell divisions. **e**, Cell cycle analysis of murine B cells 24 hours following ex vivo LPS/IL-4 stimulation. **f** Relative proportion of viable (Annexin V− PI−), early apoptotic (Annexin V + PI−) and late apoptotic (Annexin V + PI +) murine B cells before and 24 h or 48 h after ex vivo LPS/IL-4 stimulation. **g** Mitochondrial ROS level in murine B cells at baseline and 72 h after ex vivo LPS/IL-4 stimulation. Average MFI for negative control (DMSO): 10.5 (No LPS/IL-4), 136 (LPS/IL-4 at 72 h). **h** Differential sensitivity of murine B cells to parthenolide. Inset: parthenolide EC_{50} across comparator groups. **i** γH2AX expression in quiescent murine B cells. In (**d**–**i**), *Rps15*^{WT}, *Rps15*^{Het} and *Rps15*^{Hom} mice (3 mice per genotype, 3–6 months of age) were compared, with data displayed representing mean ± SEM. In **c**-**i**, statistical analysis was carried out using one-way ANOVA with Tukey's post-hoc multiple comparison test. Additional data are provided in Supp Fig. 4d, f and g. **j** Lego plot of base-base transitions across somatic SNV calls from WGS generated from 4 diseased mice (splenocytes of *Rps15*^{Het} mice and paired T cells as germline control) (hypergeometric $p < 0.0001$). **k** Two independent, de novo mutational signatures extracted with mutSignatures from the variant calls of MDR, RPS15 +/-, and TP53 -/- leukemic cells vs normal T-cells (hypergeometric $p < 0.0001$).

γH2AX, a marker of DNA damage, in both quiescent and proliferating *Rps15*^{Hom} B cells ($p = 0.0149$ and $p = 0.016$ respectively compared to *Rps15*^{WT}), as well as in quiescent *Rps15*^{Het} B splenocytes from older (11 month old) pre-leukemic mice (p = 0.0082 compared to *Rps15*^{WT}) (Fig. 3i, Supp Fig. 5a; Supp Fig. 5b). To confirm whether DNA damage occurred as a direct result of oxidative stress, we undertook WGS of 4 CLLs arising from *Rps15*^{Het} mice. Analysis of these genomes revealed profound enrichment for A•T>C•G and C•G>T•A transversions ($p < 0.0001$) that are pathognomonic of peroxide-induced DNA damage[53,54], when compared against matched T-cell normal samples, with no other significantly enriched mutational signatures (see "Methods" and Supp Data 6) (Fig. 3j-k).

p53-mediated response to oxidative stress and DNA damage underlies the hypo-proliferative phenotype of Rps15-mutant pre-leukemic B cells

To determine whether the hypo-proliferative phenotype of *Rps15*-mutant pre-leukemic B cells is directly linked to oxidative stress, we evaluated the effect of oxidative stress reversal on B cell proliferation. In *Rps15*^{Hom} pre-leukemic B cells induced to cycle with LPS/IL-4, we observed a dose-dependent reduction in mitochondrial ROS when these cells were concomitantly treated with N-acetylcysteine (NAC), a known antioxidant (Fig. 4a). Treatment with 10 mM NAC, which suppressed ROS in *Rps15*^{Hom} B cells by 52%-73%, resulted in higher ex vivo proliferative capacity upon mitogenic LPS stimulation, consistent with a partial reversal of their hypo-proliferative phenotype (p = 0.03, Fig. 4b). In contrast, NAC treatment exerted minimal effect on the proliferative capacity of *Rps15*^{WT} B cells.

We hypothesized that the phenotype of decreased proliferation and increased apoptosis characteristic of *Rps15*^{Hom} cells in the pre-leukemic setting could be attributed to a p53-mediated response to oxidative stress and DNA damage in actively replicating cells. Ribosomal proteins are known to stabilize p53 by inhibiting the p53-targeting E3 ubiquitin ligase MDM2[24–30]; consistent with this, we observed lower levels of p53 expression in cycling (LPS-stimulated) *Rps15*^{Hom} compared to *Rps15*^{WT} B cells (Fig. 4c, $p = 0.0149$). Nevertheless, substantial induction of p53 and p21 (CDKN1A) was evident in *Rps15*^{Hom} cells upon LPS stimulation, the latter a p53-dependent cyclin-dependent kinase inhibitor that functions as a critical mediator of G1 checkpoint activity[55–57]. Indeed, we observed comparable p21 levels in cycling *Rps15*^{Hom} vs *Rps15*^{WT} cells. This was accompanied by suppressed cyclin A induction in *Rps15*^{Hom} compared to *Rps15*^{WT} B cells ($p = 0.0015$) as further evidence of reduced proliferation in *Rps15*^{Hom} cells (Fig. 4c). Collectively, these results indicate that the p53-p21 pathway remained active in cycling *Rps15*^{Hom} cells despite *Rps15* mutation.

To further delineate the role of p53 in the context of *RPS15* mutation, we functionally interrogated the double-mutant *Rps15*^{Hom}/*Trp53*^{del} mice. Consistent with a partial loss of *Trp53*, *Rps15*^{Hom}/*Trp53*^{del} pre-leukemic B cells displayed reduced p21 induction in response to LPS stimulation compared to *Rps15*^{Hom} B cells ($p = 0.0055$, Fig. 4d). Accordingly, *Rps15*^{Hom}/*Trp53*^{del} B cells exhibited reduced G1 cell cycle checkpoint activity compared to *Rps15*^{Hom} B cells (p = 0.0265, Fig. 4e). This resulted in higher ex vivo proliferative capacity in *Rps15*^{Hom}/*Trp53*^{del} vs *Rps15*^{Hom} B cells ($p = 0.0059$, Fig. 4f). Indeed, the proliferative potential of *Rps15*^{Hom}/*Trp53*^{del} cells was comparable to *Rps15*^{WT} cells consistent with a reversal of the hypo-proliferative phenotype associated with *Rps15* mutation. Corroborating our ex vivo data, aged *Rps15*^{Hom}/*Trp53*^{del} pre-leukemic mice showed higher proportion of B cells in the peripheral blood compared to their *Rps15*^{Hom} counterparts ($p = 0.03$, Fig. 3c). Moreover, consistent with the role of p53 as a critical protective barrier against genomic insults, pre-leukemic *Rps15*^{Hom}/*Trp53*^{del} B cells displayed potentiation of DNA damage ($p = 0.009$, Fig. 4g) and oxidative stress ($p = 0.0015$, Fig. 4h) to levels beyond those seen in *Rps15*^{Hom} B cells. Thus, notwithstanding lower p53 expression in *RPS15*-mutant cells, these findings highlight the functional importance of residual p53 activity in the context of *RPS15* mutation that likely underlies the selective pressure for its subsequent loss through *TP53* mutation and/or deletion.

Defective DNA damage response in Rps15-mutant pre-leukemic B cells may precipitate genomic instability and transition towards a hyper-proliferative state

Given the hypo-proliferative effects of *Rps15* mutation, we sought to better characterize the mechanisms present at the pre-leukemic stage that might eventually tilt the balance towards a hyper-proliferative or malignant state. Since heightened oxidative stress and DNA damage accumulation are key phenotypic features of pre-leukemic *Rps15*^{Hom} B cells, we reasoned that these cells were hyper-dependent on the DNA damage response. Conversely, defective DNA damage response would precipitate genomic instability and confer susceptibility to the acquisition of additional genomic events such as *TP53* loss that could drive cells towards hyper-proliferation. We therefore asked whether pre-leukemic *Rps15*^{Hom} B cells could effectively respond to further genomic insults.

To address this, we assessed cellular response to hydroxyurea (HU) which induces replication stress, and ionizing radiation (IR) which induces DNA double-strand breaks (DSBs). In both *Rps15*^{WT} and *Rps15*^{Hom} B splenocytes, we observed G1- and G2/M-phase cell cycle arrest in response to HU and IR, respectively, but proportionately fewer *Rps15*^{Hom} cells underwent G2/M arrest in response to IR compared to *Rps15*^{WT} cells ($p = 0.044$ at 6 h after IR, Fig. 5a, Supp Fig. 5c, d).

https://doi.org/10.1038/s41467-026-70655-1

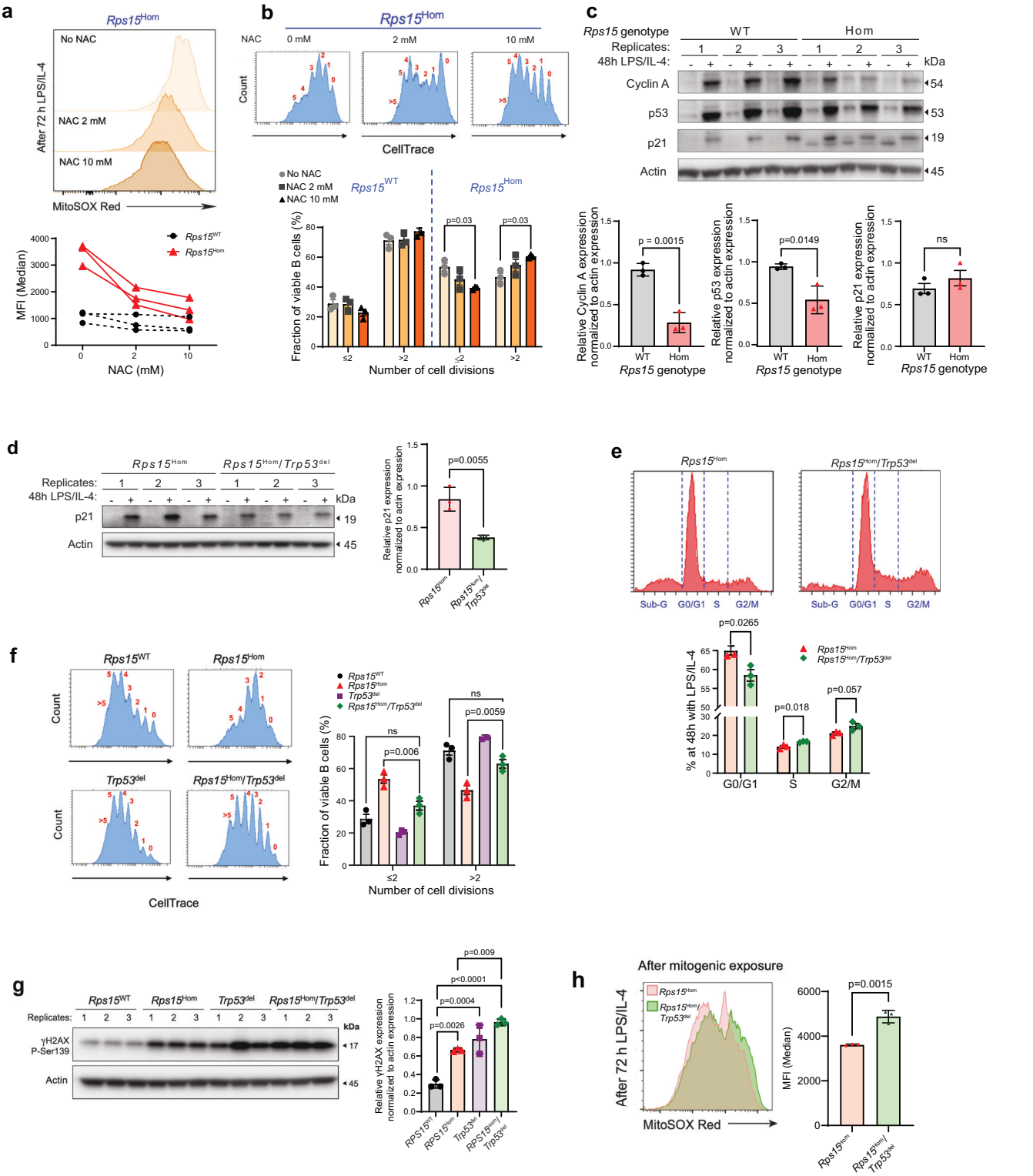

Fig. 4 | p53-mediated response to oxidative stress and DNA damage underlies the hypo-proliferative phenotype of *Rps15*-mutant pre-leukemic B cells. **a** Mitochondrial ROS level in B cells from *Rps15*^{Hom} mice 72 h after ex vivo LPS/IL-4 stimulation, with and without co-treatment with N-acetylcysteine (NAC; 2 mM or 10 mM). **b** Proliferative potential of B cells from *Rps15*^{Hom} mice 72 h after ex vivo mitogenic stimulation with LPS/IL-4, with and without co-treatment with NAC (2 mM or 10 mM). Histogram peaks show the number of cell divisions. **c** Magnitude of p53, p21 and cyclin A induction across the *Rps15* genotypes in B cells induced to cycle with LPS/IL-4 (48 hours). **d** Impact of *Trp53*^{del} on p21 induction in cycling *Rps15*^{Hom} B cells across the *Rps15* genotypes. **e** Cell cycle analysis of B cells from *Rps15*^{Hom}/*Trp53*^{del} and *Rps15*^{Hom} mice 48 h following ex vivo LPS/IL-4 stimulation. **f** Proliferative potential of B cells from *Rps15*^{WT}, *Rps15*^{Hom}, *Trp53*^{del} and *Rps15*^{Hom}/*Trp53*^{del} mice 72 h after ex vivo mitogenic stimulation with LPS/IL-4. **g** γH2AX expression in B cells from *Rps15*^{WT}, *Rps15*^{Hom}, *Trp53*^{del} and *Rps15*^{Hom}/*Trp53*^{del} mice. **h** Mitochondrial ROS level in B cells from *Rps15*^{Hom}/*Trp53*^{del} and *Rps15*^{Hom} mice 72 h after ex vivo LPS/IL-4 stimulation. In Fig. 4, 3 mice per genotype (3–6 months of age) were compared, with data displayed representing mean ± SEM. Statistical analysis was carried out using unpaired two-tail t-test (**c**–**e**, **h**) or one-way ANOVA with Tukey's post-hoc multiple comparison test (**b**, **f**, **g**).

https://doi.org/10.1038/s41467-026-70655-1

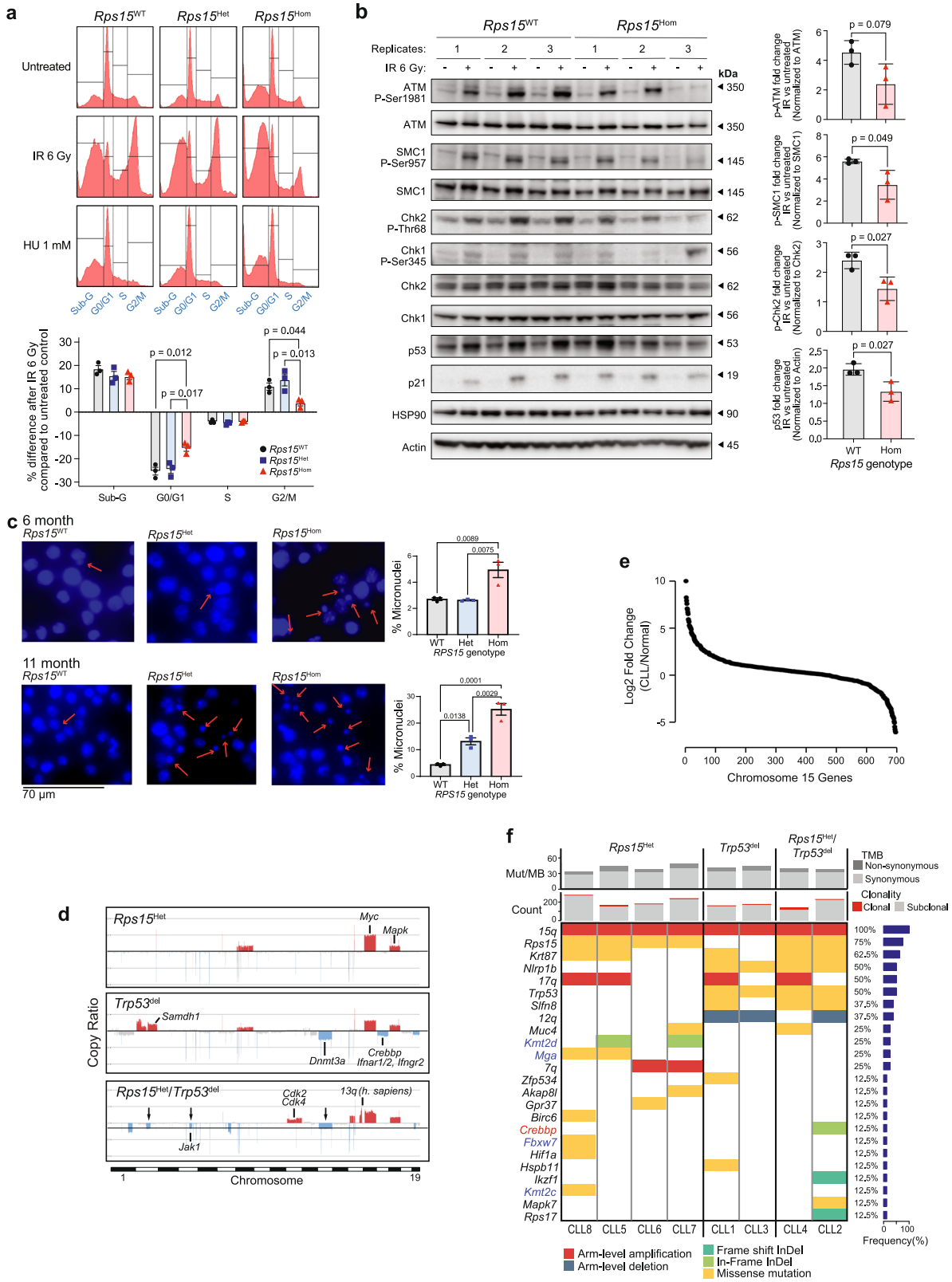

Moreover, while Chk1 response to HU was preserved in *Rps15*^{Hom} cells, Chk2 response to IR was diminished (Supp Fig. 5e). Given that DSBs frequently arise from ROS-induced DNA damage and represent the most deleterious of DNA lesions[58–62], their effective resolution is critical for the prevention of genomic instability. We therefore examined the integrity of the ATM-Chk2 pathway, which is essential for high-fidelity repair and resolution of DSBs. In *Rps15*^{Hom} B cells, we observed diminished ATM phosphorylation, diminished phosphorylation of downstream ATM targets including SMC1 and Chk2, and decreased p53 induction following IR compared to *Rps15*^{WT} cells ($p = 0.049$, $p = 0.027$ and $p = 0.027$, respectively for p-SMC1, p-Chk2 and p53, Fig. 5c). This was particularly pronounced in one of the *Rps15*^{Hom} mice (Replicate 3) where abrogation of ATM-Chk2 signaling was evident with compensatory Chk1 activation in response to IR. Taken together,

Fig. 5 | *Rps15*-mutant pre-leukemic B cells and murine CLL-like tumors display DNA damage response defects and genomic instability. a Cell cycle profiles of B cells from *Rps15*^{WT}, *Rps15*^{Het} and *Rps15*^{Hom} mice (3–6 months old) at baseline and 6 h following treatment with IR (6 Gy) or HU (1 mM). **b** ATM-Chk2-p53/p21 signaling pathway in B cells from *Rps15*^{WT} and *Rps15*^{Hom} mice (3–6 months old) with and without treatment with IR (6 Gy). **c** Micronuclei (red arrows) in *Rps15*^{WT}, *Rps15*^{Het} and *Rps15*^{Hom} splenic B cells (3–6 months old [upper panel] or 11 months old [lower panel]) cultured ex vivo for 72 h with LPS/IL-4. A minimum of 1000 B cells were evaluated per mice. In Fig. 5 a-c, 3 mice per genotype were compared, with data displayed representing mean ± SEM. Statistical analysis was carried out using one-way ANOVA with Tukey's post-hoc multiple comparison test. **d** Copy-number analysis of *Rps15*^{Het} ($n = 4$), *Trp53*^{del} ($n = 2$) and double mutant (*Rps15*^{Het}/*Trp53*^{del}) (n = 2) diseased cells. Seven of 8 animals had CLL-like disease (all *Rps15*^{Het} and *Trp53*^{del}, and 1 of 2 double mutant mice); 1 of 8 had RS-like disease (*Rps15*^{Het}/*Trp53*^{del}). Signal was combined across samples. Red: amplifications, Blue: recurrent deletions. Arrow: events unique to RS-like disease. Genes of interest highlighted within affected regions (GISTIC2.0 q-value < 0.25). **e** Changes in gene expression of Chr15 genes between CLL (from *Rps15*^{Het} mice) and normal B cells (from *Rps15*^{WT} mice). Genes were sorted by CLL/normal expression $\log_2$fold change. **f** Co-mutation plot showing mutations (allelic frequency >10%) identified across CLL and RS/DLBCL murine samples (*Rps15*^{Het}, $n = 4$; *Trp53*^{del}, $n = 2$; *Rps15*^{Het}/*Trp53*^{del}, $n = 2$). Right histogram: percent of samples with a given mutation. All missense mutations were determined to be likely damaging per SIFT scoring. Top histogram: Tumor mutational burden (TMB) and number of mutations per sample. Blue font: genes associated with DNA damage repair; Red font: genes associated with Richter's transformation. CLL2 = RS/DLBCL.

these findings support the notion that DNA damage response is aberrant in *Rps15*^{Hom} cells.

We also considered the contribution of oncogenic drivers that could support the transition of *Rps*15-mutant B cells to a hyperproliferative state by conferring additional survival and proliferative signals, allowing these cells to tolerate further increase in oxidative stress and DNA damage upon the loss of p53-dependent cell cycle regulation and apoptotic response. In addition to Myc pathway upregulation evident from our RNA-seq data, we found increased Zap70 expression in *Rps15*^{Hom} vs *Rps15*^{WT} cells, at both the transcriptional (Fig. 3b) and protein level (Supp Fig. 5f). In contrast, BCR signaling responses were more equivocal, with increased phosphorylation of Erk (p = 0.047), a late BCR signaling protein that modulates Myc[63,64], but not proximal BCR signaling proteins such as Syk, Akt and Plcγ1 in *Rps15*^{Het} or *Rps15*^{Hom} compared to *Rps15*^{WT} B splenocytes in response to anti-IgM stimulation (Supp Fig. 5g). This suggests potential involvement of recently described Zap70-mediated growth-promoting mechanisms that are not necessarily dependent upon proximal BCR signaling activity [65,66].

Rps15-mutant pre-leukemic B cells and murine CLL-like tumors display heightened genomic instability

To establish whether oxidative stress, DNA damage and defective DNA damage response collectively result in heightened genomic instability in *Rps15*-mutant pre-leukemic B cells, we compared the frequency of appearance of micronuclei in *Rps15*^{WT} and pre-leukemic *Rps15*^{Hom} splenic B cells following 72-h ex vivo mitogenic stimulation with LPS. Micronuclei results from the sequestration of DNA within aberrant extranuclear structures and is a recognized hallmark of chromosomal instability[67,68]. We discovered higher proportions of B cells harboring micronuclei in older (11-month-old) pre-leukemic *Rps15*^{Hom} and *Rps15*^{Het} pre-leukemic mice compared to *Rps15*^{WT} mice (25% for *Rps15*^{Hom} and 13% for *Rps15*^{Het} vs 4% for *Rps15*^{WT}, $p < 0.0001$; Fig. 5c), indicating heightened genomic instability in these cells.

Furthermore, to determine the burden of additional genomic alterations as a surrogate marker for genomic instability in CLL-like tumors arising from *Rps15*-mutant mice, we undertook WGS of malignant cells isolated from *Rps15*^{Het} ($n = 4$) or *Trp53*^{del} mice (n = 2) harboring CLL-like disease, as well as from *Rps15*^{Het}/*Trp53*^{del} mice with CLL-like (n = 1) or RS-like tumors ($n = 1$). Across all 8 mice, we observed the acquisition of multiple structural variants that reflects genomic instability, including recurrent amplifications of chromosomes 15 (8 of 8 mice) and 17 (4 of 8 mice) encompassing *Myc* and *Mapk*, respectively (Fig. 5d, Supp Fig. 6a). In both *Rps15*- and *Trp53*-mutant CLL-like tumors, we observed amplifications of chromosome 7 that shares homology with human chromosome 19, and these lesions mirror chromosome 19 amplifications or trisomies that have been reported as putative drivers in human CLL[8]. Unique to *Trp53*-mutant CLL-like tumors were amplifications of chromosome 2 and deletions of chromosome 12 involving the CLL drivers *Samhd1* and *Dnmt3a*, respectively[69]. Consistent with their heightened chromosomal instability, *Rps15*^{Het}/*Trp53*^{del} CLL-like tumors exhibited even more extensive copy number alterations, and uniquely harbored focal deletions of chromosome 4 (*Jak1*), amplifications of chromosome 10 (*Cdk2* and *Cdk4*) and a focal amplification on chromosome 14. *CDK2* and *CDK4* are localized to human chromosome 12 and duplicated in trisomy 12, the latter being among the most frequent lesions in RS alongside *MYC* and *MAPK* amplification. In line with the copy number increase noted in chromosomes 7, 15, and 17 of *Rps15*^{Het} mice, most of the genes on these chromosomes were upregulated in CLL cells compared with normal B cells (Fig. 5e, Supp Fig. 6b). The double mutant RS mouse had unique arm-level deletions at chromosomes 2, 4, and 12 relative to the double mutant CLL mouse, conferring deletions of *Jak1* and *Dnmt3a* (Fig. 5d).

We further identified numerous non-synonymous coding somatic single-nucleotide variants (sSNVs) across all 8 mice whose mutations were predicted to have functional impact with deleterious SIFT classification (score<0.05) (Fig. 5f). Of note, mutations in genes with high SIFT scores included putative CLL drivers such as *Kmt2c*[70], *Kmt2d*[71], *Mga*[72,73] and *Fbxw7*[74,75], each known to play key roles in DNA damage response in other cancers. *MGA* and *FBXW7* are also known negative regulators of the Myc pathway[76–78], and deleterious mutations in these genes could potentially contribute to overwhelming any existing checks and balances on already upregulated Myc activity in *Rps15* mutated cells. Further, these genes were present at high allelic frequency within their respective murine hosts (Supp Fig. 6c), suggesting that they play a key role in contributing to *Rps15*-mutant leukemogenesis, possibly as second hits. Finally, several sSNVs were unique to the DLCBL-like cells, including *Crebbp*, a gene recurrently mutated in human RS [79,80].

RPS15 mutations impair ribosome biogenesis

To uncover the relationship between ribosomal alterations and the distinct phenotypic properties of *RPS15*-mutant B cells, we turned our focus to investigating ribosomal defects secondary to *RPS15* mutation. Specifically, to directly determine if *RPS15* mutation generated changes in intrinsic ribosome function that could impact the stability of RPS15 itself as well as ribosome synthesis and assembly, and that could in turn instigate the cell cycle dysregulation and genomic instability that we observed, we used a doxycycline-inducible transposon system to stably introduce the S138-*RPS15* mutation as Flag- and HA-tagged proteins into the HG3 CLL cell line (which harbors *del*^{13q} but has intact *TP53*). Further, we used the CRISPR-Cas9 editing system to generate *TP53* knock-out (hereafter referred to as *TP53* deleted) HG3 cell lines expressing the recurrent *RPS15* mutations (Fig. 6a, Methods). To evaluate the consistency of the effects we observed, we also generated lines to model 3 other common *RPS15* mutations (*G134R, H137Y*, and *S139F*).

Recent reports in HEK293T and MEC1 (a *TP53*-mutated CLL-like cell line) suggest that *RPS15* mutations alter the stability of the mutant protein via ubiquitin-dependent proteasomal degradation[34]. In our genetically engineered HG3 cell lines, we similarly observed reduced

https://doi.org/10.1038/s41467-026-70655-1

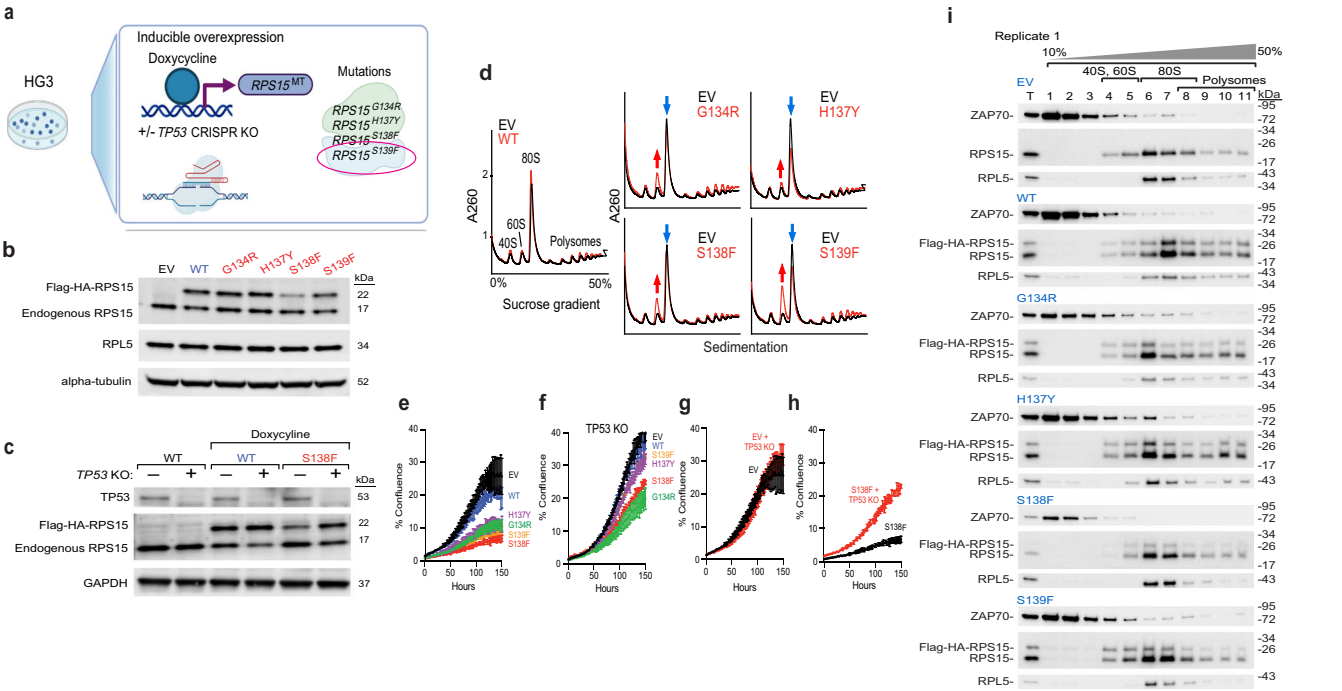

Fig. 6 | *RPS15*-mutated cells exhibit altered ribosome biogenesis and hypo-proliferation. a Diagram demonstrating gene editing approach of the Flag-HA-*RPS15* doxycycline inducible HG3 cell lines harboring 4 *RPS15* mutations identified in CLL. Circled—the mutation modeled by our gene-edited mice. Created in BioRender. Gutierrez, C. (2025) https://BioRender.com/8kf56if. **b** Western blot analysis of endogenous and transgene RPS15 protein levels in Flag-HA-*RPS15* inducible HG3 cell lines following 48 h of doxycycline induction. **c** Western blot analysis of endogenous and transgene RPS15 protein levels in Flag-HA-*RPS15* inducible, *TP53* deleted HG3 cell lines following 48 h of doxycycline induction. **d** Chromatogram of HG3 lysates in 10–50% sucrose density gradient with continuous monitoring of absorbance at 260 nm. Black - empty vector (EV); red—WT or MT. **e**–**h** Live-cell imaging quantification of cell proliferation over 150 h (3 biological replicates per condition; colors denote respective mutant cell lines; data are presented as mean values ± SD). Direct comparison of EV (**g**) and S138F MT cell lines (**h**) in the presence and absence of *TP53*. **i** Western blot analysis of cell fractions post-ultracentrifugation over sucrose gradient to separate ribosomal units and polysomes from total cell lysates. T, total unfractionated lysate. RPL5, which also incorporates in the 80S mature subunit, was used as a positive control. Additional replicates shown in Supp Fig. 7i.

levels of RPS15 protein, but not mRNA, in two of the 4 *RPS15* mutated cell lines (*RPS15*-S138F and *RPS15*-S139F) relative to the wild-type RPS15 line (Fig. 6b, Supp Fig. 7a). Given the central role of p53 in cellular stress responses[22], we asked whether *TP53* deletion might result in RPS15 protein stabilization. We noted that *TP53* deletion resulted in increased overall expression of transgene mRNA (Supp Fig. 7b, c). Yet, while we observed that *TP53* deletion rescued RPS15 protein expression, it did not rescue mRNA expression of RPS15 mutants (Fig. 6c, Supp Fig. 7b-d).

RPS15 has several essential functions in the cell, including entering the nucleolus to facilitate maturation of ribosomal RNA precursors, and mediating the final stages of ribosome maturation (namely, of the small 40S subunit) and assembly in the cytoplasm. Consistent with prior studies in HEK293T[34], our HG3 CLL-like line analyses indicated that RPS15 mutant protein, like RPS15 WT protein, is distributed mainly in the cytoplasm and nucleolus, as determined by immunofluorescence (Supp Fig. 7e). Thus, the *RPS15* mutations we modeled do not impede nuclear import and export of RPS15.

To evaluate whether *RPS15* mutation impacts ribosome maturation, we performed polysome tracing of the HG3 mutant lines. Analysis of both empty vector and wild-type overexpression showed a classical profile of ribosomes and polysomes (Fig. 6d-left), with similarly sized small peaks representing the 40S (small) and 60S (large) ribosomal subunits, a large peak representing the 80S mature assembled ribosome (monosome), and subsequent peaks representing polysomes. However, all four *RPS15* mutant lines resulted in increased amounts of free 60S subunits and reduced amounts of mature 80S ribosomes (Fig. 6d-right, Supp Fig. 7f), indicating a likely deficit in 40S maturation that results in accumulation of excess 60S and reduced mature ribosome assembly.

Since studies in yeast have demonstrated a similar phenotype upon RPS15 depletion[37,81–83], we examined if mutant RPS15 was stable enough to co-localize with and incorporate into mature ribosomes. By using sucrose gradient centrifugation to separate free protein and pre-ribosomal particles from mature ribosomes and polysomes, and immunoblotting of individual fraction lysates, we observed that Flag-HA-tagged RPS15 mutants were present in the small subunit and mature ribosome fractions (Supp Fig. 7g). The ability of RPS15 mutants to incorporate into the ribosome, and the localization of RPS15 mutants specifically to the C-terminus tail which engages the ribosome decoding center[84–86], all underscore a likely direct impact on ribosome function.

Finally, we evaluated the impact of RPS15 mutants on CLL cell growth. Consistent with our in vivo studies, we confirmed that the *RPS15*-mutant HG3 cells proliferated more slowly than empty vector and wild-type-overexpressing cells, as measured by live-cell imaging (Fig. 6e, Supp Fig. 7h-top, Methods). By contrast, *TP53*-deleted cells exhibited more rapid growth across all *RPS15* mutants (Fig. 6f) and were most apparent in the S138F mutant line (Fig. 6g-h, Supp Fig. 7h-bottom). Since direct interaction between ZAP70 and the ribosome has been described[65], we asked whether mutant RPS15, given its disruptive role in ribosome synthesis, might impact ZAP70 and ribosome interactions. Through immunoblotting of ZAP70 levels across the small and large ribosomal subunits, mature ribosomes, and polysomes isolated from HG3 lysates, we indeed observed ZAP70 in ribosomal fractions, and further that *RPS15* mutation did not ablate this interaction (Fig. 6i, Supp Fig. 7i).

https://doi.org/10.1038/s41467-026-70655-1

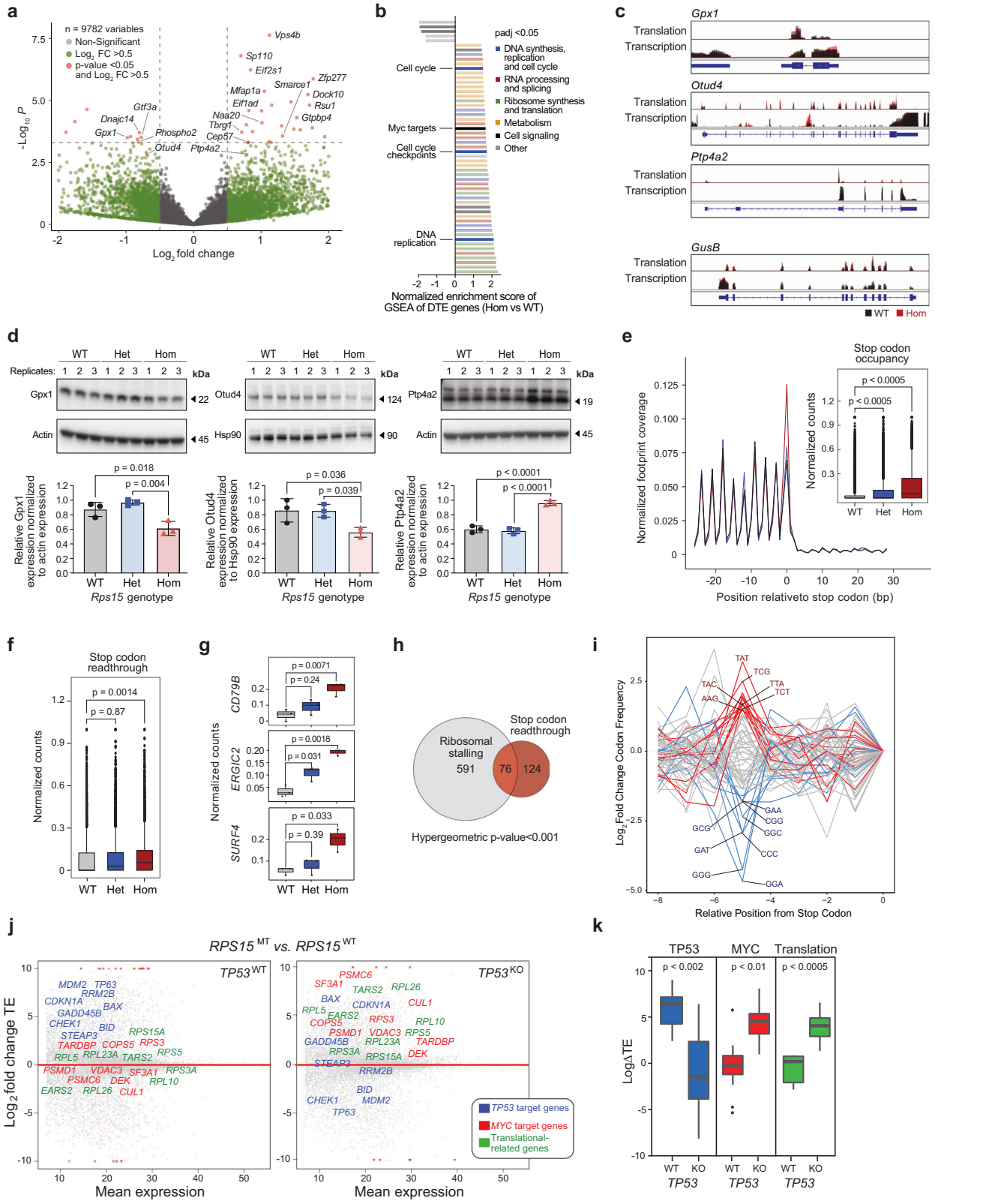

RPS15-mutant ribosomes exhibit altered translation via changes in translation efficiency, ribosome stalling, and stop codon readthrough that result in cellular phenotype alterations

In CLL, *RPS15* mutations occur in the C-terminal tail of RPS15, a region purported to interact with the A- and P-site tRNAs during translation[84,85]. To determine whether *RPS15*-S138F impacts translation efficiency (TE), we performed ribosome profiling of *Rps15*^{WT}, *Rps15*^{Het}, and *Rps15*^{Hom} pre-leukemic B cells from 3–6-month-old mice. By comparing levels of ribosome-associated mRNA (ribosome footprints) against the total mRNA levels present for each gene, we identified 342 genes with differential TE between *Rps15*^{Hom} vs *Rps15*^{WT} cells (222 increased, 120 decreased; $\log_2FC > 1.5$, $p < 0.05$ with DESeq2 FDR-adjusted two-sided Wald tests; Fig. 7a, Supp Data 7). By GSEA, these were predominantly involved in DNA replication, cell cycle

Fig. 7 | *RPS15* mutation drives changes in translational efficiency, ribosome stalling, and stop codon read-through of select mRNA transcripts. In Fig. 7a-i,k, 3 mice per genotype were compared, all 3-6 months old. Statistical analysis was carried out with two-sided Welch's t-tests, unless otherwise indicated. Boxplots represent the interquartile range, split by the mean, with outliers shown. **a** Volcano plot of DTE genes in *Rps15*^{Hom} pre-leukemic vs *Rps15*^{WT} murine B cells (log2FC > 0.3, DESeq2 two-sided Wald test Benjamini-Hochberg FDR-adjusted $p < 0.05$). Red=-MYC target genes; Blue=Cell cycle genes. **b** Barplot depicting GSEA of DTE genes in *Rps15*^{Hom} pre-leukemic vs *Rps15*^{WT} murine B cells from *Rps15*^{WT} (FDR-adjusted two-sided empirical $p < 0.05$, normalized enrichment score (NES) > |1.5|). **c** Confirmatory IGV screenshots for example genes (*Gpx1, Otud4, Ptp4A2*) with DTE and a house-keeping gene (*GusB*) show differences in ribosome-protected mRNA fragment (RPF) counts (top) juxtaposed with differences in transcript counts (bottom) between *Rps15*^{Hom} and *Rps15*^{WT} tumors. **d** Purified B cells from *Rps15*^{WT}, *Rps15*^{Het} and *Rps15*^{Hom} mice, confirming downregulation of Gpx1, Otud4 and Ptp4a2 in *Rps15*^{Hom} vs *Rps15*^{WT} mice. Quantification of signal across replicates (bottom) with mean ± SEM annotated. Statistical analysis was carried out using one-way ANOVA with Tukey's post-hoc multiple comparison test. **e** Boxplots of RPF density over positions surrounding stop codons across genotypes (black = *Rps15*^{WT}; blue=*Rps15*^{Het}, red = *Rps15*^{Hom}). RPF counts were normalized by library size. Inset=Boxplots display distributions of normalized RPF counts downstream of stop codons across genes with stop codon readthrough: $p = 2.9 \times 10^{-15}$, *Rps15*^{WT} vs *Rps15*^{Het}; $p = 9.42 \times 10^{-33}$, *Rps15*^{WT} vs *Rps15*^{Hom}. **f** Boxplots of counts of footprints overlapping the region 1–30 bp past the stop codon across all genes. **g** Boxplots of individual genes with stop codon readthrough (DESeq2 $p < 0.05$). **h** Venn diagram depicting overlap of genes with evidence of ribosome stalling and stop codon readthrough. **i** Line-plot depicting the $\log_2$fold change in codon usage over 29-nucleotide spans upstream of the stop codons of canonical protein-coding regions (667 genes with ribosome stalling vs 961 control genes, Benjamini-Hochberg adjusted $p < 0.25$). **j** MA plots of DTE genes in *RPS15*^{S138F} vs *RPS15*^{WT} HG3 cells, *TP53*^{WT} (left) or *TP53*^{KO} (right) conditions. **k** Boxplots of DTE values for *RPS15*^{S138F} vs *RPS15*^{WT} across gene sets (blue=*TP53* pathway, red=Myc targets, green=translation), in *TP53*^{WT} or *TP53*^{KO} conditions. (TP53 pathway $p = 0.00178$, Myc targets $p = 0.01151$, translation $p = 6.751 \times 10^{-6}$).

checkpoints, RNA processing, ribosome synthesis and translation, metabolism, and cell signaling (GSEA FDR-adjusted two-sided empirical p < 0.05, NES > 1.5; Fig. 7b). A subset of genes with differential TE were confirmed by manual inspection via the Integrated Genomics Viewer (IGV)[87] (Fig. 7c; Supp Fig. 8a, b).

We examined potential mechanisms through which differential TE could contribute to the distinct phenotype of *Rps15*-mutant cells. We prioritized a representative set of the most significantly enriched targets by differential TE analysis, for which we also confirmed altered expression by RNAseq (Supp Data 8-last tab) and through proteomic analysis of samples of matched genotype (Methods, Supp Data 9), which we then selected for validation by western blotting. Among proteins with confirmed downregulation in *Rps15*^{Hom} cells secondary to reduced TE was Gpx1, a glutathione peroxidase that functions as a key cellular antioxidant by scavenging hydrogen peroxide (Fig. 7a, c, d; Supp Fig. 8b)[88]; decreased Gpx1 expression may therefore potentiate oxidative stress and DNA damage in *Rps15*^{MT} cells. Also significantly downregulated in *Rps15*^{Hom} cells as a consequence of translational buffering was Otud4, a de-ubiquitinase that promotes the base-excision repair of alkylation-induced DNA adducts (Fig. 7a, c, d; Supp Fig. 8b)[89]. Other DNA repair genes with reduced TE in *Rps15*^{Hom} cells included Smarca2, a chromatin remodeler critical for non-homologous end joining and homology-directed repair of DSBs[90–94], *Fance*, a component of the Fanconi anemia complex[95,96], and *Tlk1*, a mediator of DSB repair[97,98], which could potentially result in their decreased protein expression, thereby exacerbating DNA damage and genomic instability. In contrast, important genes regulating cell cycle progression (*Ptp4a2*[99], *Gtpbp4*[100], *Tbrg1*[101]) and translation initiation (*Eif1ad*) had increased TE in *Rps15*^{Hom} cells, with resultant protein upregulation of Ptp4a2 and Eif1ad confirmed by western blotting (Fig. 7a, c, d; Supp Fig. 8a-c); we speculate that these likely shape altered cellular response to DNA damage and govern their transition from a hypoproliferative to a hyperproliferative state.

Notably, we observed marked ribosome accumulation at stop codons in *Rps15*^{Hom} B cells, suggestive of ribosome stalling (Fig. 7e). This was evident in *Rps15*^{Het} and even more so in *Rps15*^{Hom} B cells, compared to *Rps15*^{WT} (Wilcoxon two-side test $p < 0.0005$, 90 and 667 differential stalling genes in Het and Hom samples, respectively; DESeq2 FDR-adjusted two-sided Wald test $p < 0.25$) (Fig. 7e-inset). Ribosome stalling at termination elements can precede stop codon read-through[102], and indeed we identified increases in ribosome occupancy of regions 3–28 nucleotides downstream of the stop codon in *Rps15*^{Hom} vs wild-type cells ($p = 0.0014$; Fig. 7f). Notable mRNA transcripts exhibiting stop codon read-through included *CD79B*, a signaling component of the B-cell antigen receptor, as well as endoplasmic reticulum components integral to appropriate protein translation such as *ERGIC2* and *SURF4* (Fig. 7g, Supp Fig. 8d). 76 of 200 (38%) genes with stop codon read-through in *Rps15*^{Hom} samples were found to co-exhibit ribosome stalling (Fig. 7h), including translation-mediating genes *RPS18*, *EIF3I*, and *NUDT21* as well as genes implicated in cell cycle regulation and DNA repair.

Since mRNA sequences immediately upstream of the stop codon can impact rates of ribosome stalling and stop codon read-through[103,104], we evaluated whether mutated RPS15 was associated with differential protein codon usage on the 27-nucleotide region upstream of the stop codon. Through chi-squared testing, we uncovered localized enrichment of four codons (TAC [tyrosine], AAG [lysine], AAC [asparagine], ATG [methionine]) and depletion of four codons (GGA [glycine], CCC [proline], TGC and TGT [cysteine]) in relation to the *Rps15* mutation (Benjamini Hochberg, *p*-adj <0.05; Supp Fig. 8e, Supp Data 10). Notably, while stop-codon read-through can occur via probabilistic molecular errors, most often involving the stop codon UGA[105], we did not observe significant enrichment of this codon in genes with increased stop codon read-through. Instead, codons with Levenshtein distances of ≤1 from TAG, TAA, and ATG were exclusively enriched at the 5th trinucleotide upstream of the stop codon while codons with Levenshtein distances of ≤1 from GAT, GGG were exclusively depleted (|log2 FC| > 1.5) (Fig. 7i, Supp Data 10). These data suggest that *Rps15*-mutant ribosomes preferentially stabilize interactions between stop codons and tRNAs with anticodons that are semi-complementary to stop codons, which compete with the binding of translation termination factors. Since tRNAs bound to the 5th trinucleotide are expelled from the ribosomal cleft when ribosomes translocate to the stop codon[106], the localization of enrichments to the 5th trinucleotide further suggests that stalling/read-through events are more likely to occur if semi-complementary tRNAs are in the immediate vicinity of the 5′ edge of the ribosome. While transient binding of semi-complementary aa-tRNAs to stop codons could explain *Rps15*-mutant ribosomal stalling, tRNAs which drive ribosomal translocation through stop codons are expected to be associated with elongation factors[107,108]. Consistent with the idea that association with elongation factor is a distinct rate-limiting step for readthrough but not stalling, we observed that ribosomal stalling at the stop codon occurred at a greater rate than stop codon read through in mutant *Rps15* mice (Fig. 7e). Together, these findings support the notion that stop codon stalling/readthrough depends on channeling of recently expelled, semi-complementary tRNAs back to ribosomes paused at stop codons [109–112].

Finally, to determine whether *RPS15* mutation also influences mRNA translation in leukemic B cells, and whether *TP53* deletion impacts this relationship, we performed ribosome profiling concurrently in *RPS15*-S138F mutant and WT HG3 cells with and without *TP53* (*TP53*^{WT} and *TP53*^{KO}, respectively). We identified 3,308 genes with differential TE between *RPS15* mutant vs wild-type cells, of which 1754 genes had increased and 1554 genes had decreased TE

https://doi.org/10.1038/s41467-026-70655-1

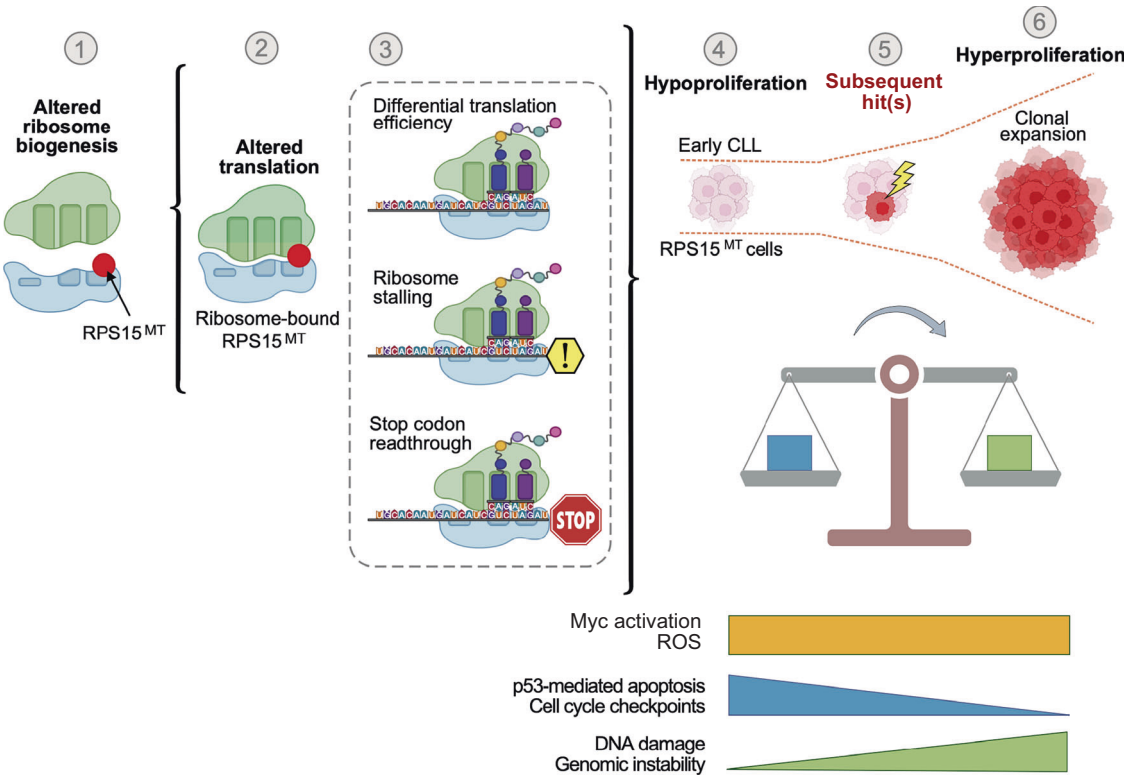

Fig. 8 | Summary schema of the mechanisms by which *RPS15* mutation sets the stage for tumorigenesis and CLL development. RPS15 mutant protein comprises the small 40S subunit of the ribosome (1) and, when incorporated into ribosomes, can alter translation efficiency, ribosome stalling and stop codon readthrough (2,3) These actions result in a balance of hypo-proliferative and hyper-proliferative signals initially favoring hypo-proliferation (4) but genomic instability that sets the stage for subsequent hits (5) that ultimately tilts the balance towards hyperproliferation and clonal expansion of *RPS15* mutant cells (6) Created in BioRender. Gutierrez, C. (2025) https://BioRender.com/0824pyn.

($\log_2$FC > 0.5, $p < 0.1$). This dysregulation was even more marked in *TP53*^{KO} cells, where we identified 3,380 genes with differential TE between *RPS15* mutant vs wild-type cells, of which 1820 genes had increased and 1560 genes had decreased TE. GSEA analysis of differentially translated genes revealed a strong enrichment of *TP53* target genes (Fig. 7j-left), consistent with activation of DNA damage and stress response pathways in *RPS15*-mutant cells. *TP53*^{KO} cells, however, exhibited a marked increase in TE of Myc target genes and components of the ribosomal machinery (Fig. 7j-right, Fig. 7k). These findings, together with our studies in murine pre-leukemic models, suggest that *RPS15* mutation sets the stage for oncogenesis through Myc signaling dysregulation, and that subsequent loss-of-function mutations in DNA damage response and cell cycle regulator genes such as *TP53* may then enable further Myc dysregulation and clonal expansion.

Discussion

Across cancers, malignant cells have demonstrated their ability to manipulate and deregulate translation to promote oncogenic activity. The concept of an 'oncogenic ribosome' has generated growing interest given the frequency of ribosomal protein mutations in cancer, the heterogeneity and plasticity reported in ribosomal composition and function, as well as its regulation of processes such as cell cycle, migration, metabolism and cell growth. How ribosomal protein mutations, which have been predominantly reported to induce hypoproliferative defects, can drive cellular transition in vivo to a disease characterized by uncontrolled cellular division remains incompletely understood.

Here, we unequivocally establish *RPS15* mutation as a CLL driver. B-cell-restricted expression of *RPS15* mutation resulted in a CLL mouse model that exhibited many of the key features of this disease, including its indolent growth (onset at >16 months of age), pathologic features, and predominant occurrence in heterozygous mutant mice. The availability of these engineered lines also provided us the opportunity to evaluate the early (pre-leukemic) impact of *Rps15* mutation in order to definitively establish the in vivo mechanisms underlying transformation to CLL. In particular, our studies delineate a cadence of events leading to the generation of malignant disease.

One of the fundamental changes generated by RPS15 mutation pertained to the contribution of RPS15 to essential functions of the ribosome, as manifested in changes in translational efficiency, ribosome stalling, and enhanced stop codon read-through of select mRNA with specific codon sequences. Given that the native *Rps15*-S138 amino acid residue localizes to the C-terminus tail of RPS15, is normally phosphorylated, and interacts with tRNAs on ribosomes, our findings suggest that mutation of serine to phenylalanine at this position results in structural/catalytic changes that affect translation efficiency and impede translation termination. These findings are supported by studies in fungi, where elements of the *RPS15* C-terminus participate in hyper-accurate stop codon recognition[113], and in *RPS15*-mutant HEK293T cells, where stop codon read-through was detected using synthetic functional studies[34]. Stalled ribosomes and stop codon read-through can both activate cellular stress pathways (such as ribosome quality control complexes and the unfolded protein response) and induce oxidative stress (ROS) that downregulate translation and regulate cellular survival[114] (Fig. 8). Further, we uncovered several genes involved in translation and protein folding with evidence of ribosome stalling and stop codon read-through (such as *ERGIC2* and *SURF4*). Given that stop codon read-through frequently results in C-terminally extended proteins with potentially deleterious effects, read-through of mRNA transcripts corresponding to core translation genes would likely have a detrimental impact on global protein synthesis and cellular function.

In addition to reduced translation fidelity, we detected numerous alterations in translation efficiency that might impact B-cell function in our pre-leukemic mouse model. *RPS15* mutations have been reported to rewire the translational program of primary CLL cells, particularly affecting translational machinery and immune processes[35]. We found that this was true even at the pre-leukemic stage, and furthermore, that key genes involved in ameliorating oxidative stress and regulating DNA damage response are detrimentally affected with reduced translation efficiency (including *Gpx1, Otud4, Smarca2, Fance, and Tlk1*, amongst others). In contrast, genes regulating cell cycle (*Ptp4a2, Gtpp4, Tbrg1*) and translation initiation (*Eif1ad*) exhibited increased translation efficiency—underscoring the complex interplay of hypoproliferative and hyperproliferative signals present in *Rps15*-mutated cells well in advance of leukemic transformation.

As would be expected given these deficiencies in translation efficiency and fidelity, pre-leukemic *Rps15*-mutated B cells exhibit decreased ribosome maturation and cellular proliferation (consistent with previous findings in HEK293T cells[34]), as well as increased ROS and activation of DNA damage response, while also exhibiting proliferative cell signals (increased ZAP70 and Myc activation) (Fig. 8). Our leukemic mouse models thus underscore that while this balance is initially weighted towards hypoproliferation, mediated in part through a p53-dependent induction of cell cycle arrest, this is ultimately insufficient to prevent the accumulation of DNA damage and genomic instability. The latter sets the stage for subsequent genetic hits that eventually reverse the quiescent cellular phenotype and tilt the cell towards hyperproliferation, as exemplified by the upregulated MYC and E2F targets and other cell cycle genes observed in murine and human leukemic cells, and *Myc* amplification in murine CLL[69,115,116]. Our findings corroborate previous studies of *RPL10*-mutated T-ALL and *RPL11* mutations Diamond-Blackfan anemia that linked cellular hypoproliferation with oxidative stress and DNA damage[16,18,33,117]. Indeed, products of DNA damage, such as the CNV and sSNVs identified in our models (many of which parallel the CNAs identified in human *RPS15* mutant CLL, Supp Fig. 1a), are likely detrimental to cell growth and proliferation. We thereby speculate that such cells undergo negative selection initially, but over time may result in a select subpopulation of cells accruing mutations that can overcome p53-mediated apoptosis and cell cycle blockade and ultimately expand. Consistent with the accumulation of such changes over time, we point to the long latency characteristic of both human CLL and murine CLL-like disease.

Also consistent with *RPS15*-mutated human CLL, which is exclusively heterozygous, mice with predominantly heterozygous, not homozygous, *Rps15* mutation developed CLL-like disease. Indeed, notwithstanding higher mitochondrial ROS, γH2AX and micronuclei levels in $Rps15^{Het}$ B splenocytes compared to their $Rps15^{WT}$ counterparts evident in older (11-month-old) pre-leukemic mice (Fig. 5c), we found substantially reduced circulating B cells in $Rps15^{Hom}$ as compared to $Rps15^{Het}$ pre-leukemic mice of younger age (6-month) (Fig. 3c), contrary to our expectation that the presence of two *Rps15* mutant alleles would confer a stronger phenotype of diminished proliferation concomitant with heightened ROS production and DNA damage. We speculate that, given that wild-type Rps15 can stabilize p53 through the Mdm2-p53 regulatory axis, which is key to ribosome surveillance and cell cycle regulation[30], complete absence of the *Rps15* WT allele in the homozygous setting may result in a less effective p53-mediated response to cellular stress and dysfunction. Moreover, excessive cellular stress and DNA damage are incompatible with cell survival and may result in more rapid cellular demise in $Rps15^{Hom}$ cells through apoptosis, ferroptosis and/or mitotic catastrophe[118,119]. Indeed, we found increased apoptosis in $Rps15^{Hom}$ B cells from pre-malignant mice compared to their $Rps15^{Het}$ and $Rps15^{WT}$ counterparts (Fig. 3f). Ultimately, reduced cell viability results in a smaller pool of pre-malignant cells and hence constituting a selective disadvantage with fewer opportunities for cells to accumulate the mutations necessary to transform – and would support why heterozygous, and not homozygous, *RPS15* mutations are predominantly observed in CLL patients and in our mouse model.

Given this, we leveraged our double-mutant cell line and mouse models to explore the relationship between *RPS15* and *TP53* co-mutation. Loss of *TP53* in our *RPS15* mutant cell lines enabled unchecked propagation of *RPS15* mutant phenotypes, including increased Myc signaling and cell proliferation. This was corroborated by our data from *Rps15*-mutant pre-leukemic mice that showed a complete reversal of the hypo-proliferative phenotype upon the concomitant loss of *Trp53*, accompanied by further potentiation in DNA damage and genomic instability (Fig. 4f), thus underlining the important role of residual p53 activity in countering the effects of mut-*RPS15*-induced DNA damage and accounting for the selection pressure for its subsequent loss through *TP53* deletion and/or mutation. Reminiscent of our findings, a previous murine model recapitulating 5q- syndrome showed *Rps14* haploinsufficiency to cause p53-induced bone marrow progenitor cell apoptosis that resulted in macrocytic anemia[120]. Intercrossing of these mice with p53-deficient mice completely rescued the progenitor cell defect, thus accounting for the frequent co-occurrence and adverse impact of *TP53* defects in myelodysplasia with isolated 5q-[121]. Likewise, *Rpl11* haploinsufficiency in a murine model of Diamond-Blackfan anemia was associated with increased basal Myc levels and decreased p53 induction[117], which we also observed in *Rps15*-mutant pre-leukemic B cells (Fig. 3b; Fig. 4c). However, our murine models demonstrate that decreased p53 induction does not translate to a complete abolition of p53 activity. On the contrary, *Rps15*-mutant B cells were highly dependent on such activity (e.g., p21-mediated G1/S cell cycle induction) for the amelioration of oxidative DNA damage essential for the maintenance of genome integrity (Fig. 4d-h), and such p53 activity was also observed in the context of *Rps14* haploinsufficiency, where p21 remained active[122]. Indeed, recent mechanistic studies highlight the intricate crosstalk between Myc and p53, where Myc overexpression induces p53-dependent apoptosis, and as a consequence, Myc-associated tumors often require disruption of the apoptosis pathway to promote cell proliferation, thereby conferring an evolutionary advantage to *TP53* loss [123].

Further, we established in mice that although *Trp53* heterozygous deletion alone can also drive CLL-like development, co-mutation of *Rps15* and *Trp53* resulted in shorter disease latency, higher prevalence of CLL-like disease in homozygous *Rps15* mutant mice, and, in some cases, development of DLBCL possibly via transformation to Richter's Syndrome. These data, alongside emerging reports of *RPS15* mutation in human RS and DLBCL[47–49], support a driving role of *RPS15* mutation in RS. Many of the deleterious sSNVs identified in our model affect DNA damage repair genes, paralleling the common co-occurrence of such mutations in *RPS15* mutant patient samples, and support our functional data that suggest DNA damage is a key mechanism by which *RPS15* mutant cells transform. These patterns underscore the deleterious impact of deficient DNA damage response pathways in RPS15-mutated CLL. Further, our analysis of patient outcomes highlights that while *RPS15*-mutated tumors alone do not result in significantly worse survival outcomes, the combination of *RPS15* and *TP53* mutations (the latter possibly acquired as a second hit) results in more aggressive disease and poorer outcomes. Given the poorer prognosis associated with *RPS15* mutations in human CLL, and the potential predisposition to Richter's Syndrome, our data also provide a rationale for including *RPS15* in targeted sequencing panels for routine clinical use.

Altogether, our *Rps15* mutant mouse model establishes that ribosomal protein mutations can drive B cell malignancy by inducing a balance of hypo- and hyper-proliferative signals. These signals initially favor cellular quiescence, but through translational rewiring, cumulative oxidative stress, and genomic instability, a stage is set for the acquisition of additional 'hits' that can overcome this cell cycle block to trigger malignant transformation. As proposed in other ribosomal

protein-mutant diseases[20,31,32], our findings collectively support a model where defective ribosomes result in perturbed cellular programs which ultimately drive malignant processes and, in this case, leukemogenesis. Given recent advances in ribosome-targeting therapy[32], our findings may enable the identification of new therapeutic vulnerabilities for ribosomopathy-associated malignancies.

Methods

Experimental model and subject details

Our research complies with all relevant ethical regulations. All patient samples were collected in accordance with the principles of the Declaration of Helsinki and with the approval of the Institutional Review Boards of Avicenne Hospital and DFCI. Patients provided samples after their informed consent, and de-identified primary human CLL samples derived from peripheral blood mononuclear cells were used.

All animals were housed at DFCI and procedures were completed in accordance with the Guidelines for the Care and Use of Laboratory Animals and were approved by the Institutional Animal Care and Use Committees at DFCI. A dark-light cycle of 12 h of light followed by 12 h of dark was used. Animals were kept at 30–70% relative humidity. A stable ambient temperature was maintained of 68–79 °F. Environmental enrichment was provided, including nesting materials

Patient samples. Primary CLL samples were obtained from Avicenne Hospital, Assistance Publique-Hôpitaux de Paris, Bobigy, France and from the CLL-map project (including patients from the German, Spanish, NHLBI, UCSD, MD Anderson and Dana-Farber Cancer Institute [DFCI] cohorts; Supp Data 1)[36,116]. Samples from the CLL-map project were collected as previously described[36]. For samples from Avicenne Hospital, informed consent was obtained from all subjects and specimens were collected in accordance with the principles of the Declaration of Helsinki and with the approval of the Institutional Review Boards of Avicenne Hospital and DFCI. Tumor samples were collected upon diagnosis and prior to therapy. Fresh CLL cells were isolated from peripheral blood via Ficoll, and flow cytometry analysis confirmed tumor purity of >80% in all cases. All blood samples underwent *IGHV* sequencing for the assessment of *IGHV* mutational status, conventional cytogenetics, fluorescence in-situ hybridization (FISH) analysis of trisomy 12, 11q, 13q and 17p deletions, and amplicon-based next-generation sequencing of CLL-related mutated genes (*TP53*, *NOTCH1*, *SF3B1*, *FBXW7*, *RPS15*, *POT1*, *MYD88*, *BIRC3*, *ATM* and *XPO1*).

Mouse models. *Rps15*-S138F floxed mice (C57BL/6 background) were generated (Biocytogen, MA) by flanking endogenous WT exons 3, 4 and a stop codon with Lox-P sites, followed by exons 3 and 4 with the *RPS15*-S138F point mutation knocked-in to exon 4. In the presence of the recombinase flippase (Flp), the neomycin/lacZ cassette, flanked by flippase recognition target (Frt) sites, was flipped out. Subsequently, in the presence of Cre recombinase, the sequence between the LoxP sites is removed, allowing for the expression of the *Rps15* mutant allele. *Trp53*^{del} mice (B6.129P2-Trp53$^{tm1Brn/J}$) were purchased from the Jackson Laboratory.

To obtain B cell-specific expression, *Rps15*-S138F floxed mice and *Trp53* heterozygously deleted floxed mice were crossed with *Cd19*-Cre/Cre mice (JAX stock #006785) to generate *Cd19*-Cre/+ *Rps15*-S138F fl/+ (*RPS15*^{Het}) and *Cd19*-Cre/+ *Trp53-del* fl/+ (*Trp53*^{het}) mutant mice, respectively. These heterozygous mutant mice were further crossed to generate homozygous mice (*Cd19*-Cre/+ *Rps15*-S138F fl/fl or *Cd19*-Cre/+ *Trp53-del* fl/fl, respectively).

To generate *Rps15*^{MT} /*Trp53*^{del} mice, *Cd19*-Cre/+ *Trp53-del* fl/fl and C57BL/6 mice (JAX stock #632) were crossed to generate *Cd19*-Cre/+ *Trp53-del* fl/+ *Rps15* +/+ mice, and *Cd19*-Cre/+ *Rps15*-S138F fl/fl and *Cd19*-Cre/+ *Trp53-del* fl/fl were then further crossed to generate *Cd19* Cre/+ *Trp53* fl/+ *Rps15*-S138F fl/+ and *Cd19* Cre/+ *Trp53*fl/+ *Rps15*-S138F fl/fl (*RPS15* WT, heterozygous and homozygous) mice.

In all cases, genotypes were confirmed by PCR of tail gDNA using a set of primers targeting the floxed allele:

Rps15 Forward: 5′-GCAAGCGCTCTAGATTGTGACCTC
Rps15 Reverse: 5′-CTCTAAAATGAATCCACCAGCTTCCAC
Trp53 Forward: 5′-GGTTAAACCCAGCTTGACCA
Trp53 Reverse: 5′-GGA GGC AGA GAC AGT TGG AG

Activation of the floxed allele by Cre recombinase was confirmed by PCR on gDNA from purified B cells and non-B cell fractions using a set of primers that amplifies the activated allele:

Cre-activated Forward: 5′-GCAAGCGCTCTAGATTGTGACCTC
Cre-activated Reverse: 5′-GGAGACTGAGGCAGATCTGTCGAC

This reaction amplifies the target-activated allele at 142 bp. Presence of the activated allele was only detected in the purified B cell fraction. The following mice will be available from The Jackson Laboratory: *Cd19*-Cre/Cre *Rps15*-fl/fl (JAX #037632).

Method details

Clinical outcome modeling. Overall survival was calculated as the time from the date of the sequenced sample to the date of death and censored at the date last known alive. FFS was calculated for treatment-naive patients as the time from the date of the sequenced sample to the date of first treatment ('natural progression'), progression (if the patient was sampled at the time of enrollment on a clinical trial) or death, and censored at the last known event-free date. Univariate and multivariable Cox regression models were constructed for each subset of data. Final models were selected using the glmnet function for regularized Cox regression using an elastic net penalty within the Coxnet package in R. Tenfold cross-validation using the cv.glmnet function with a partial-likelihood deviance metric to minimize λ was performed and the minimum CV-error model was used. The alpha was set to 1, corresponding to a Lasso penalty. The maximum iterations (maxit) parameter was set to 1000. Features identified as having non-zero coefficient values using elastic net and selected in the final model were then included in a Cox regression model to obtain hazard ratios. These hazard ratios estimate the magnitude of effect, but P values and confidence intervals are not readily interpretable in the elastic net model and are therefore not reported. The Breslow approximation was used for handling ties in survival time.

Pyrosequencing. Relative transcript expression of the *RPS15* mutant allele compared to the wild-type was quantified by cDNA pyrosequencing as previously described[115]. Biotinylated amplicons were generated via cDNA synthesis and PCR amplification of transcripts surrounding the site of *RPS15*-S138F human and mouse mutation. Immobilized biotinylated single-stranded DNA fragments were isolated per the manufacturer's protocol (Pyromark Gold Q96, Qiagen) and sequenced using an automated pyrosequencing instrument (PSQ96, Qiagen). The following primer sequences were used for amplification and pyrosequencing of the human and mouse cDNA, respectively:

Human forward PCR primer: 5′-ACAAACCCGTGAAGCATGG
Human reverse PCR primer: 5′Biotin-TACTTCAGGGGGATG AATCTGG
Human pyrosequencing probe: 5′-ATAGGGGCAACACACT
Mouse forward PCR primer: 5′-CCTACAAACCCGTGAAGCA
Mouse reverse PCR primer: 5′Biotin-TTGAGGGGGATGAATCGG
Mouse pyrosequencing probe: 5′-TCGGTGCCACCCACT

Quantitative analysis was performed using Pyrosequencing software from Qiagen.

Monitoring of disease in peripheral blood. Mice were monitored monthly from 3 to 24 months of age. Peripheral blood (100 μL) was

collected from mice via submandibular bleeds into EDTA-coated tubes. Erythrocyte lysis was performed by incubating blood samples in 1 mL of ACK buffer for 5 min and subsequently washed with PBS supplemented with 2% FCS and 2 mM EDTA. Cells were then stained with a cocktail of antibodies targeting CD5 (anti-CD5-FITC, Biolegend #100606), B220 (anti-B220-PacBlue, Biolegend #103227), CD11b (anti-CD11b-APC, Biolegend #101225), CD3 (anti-CD3-APC-Cy7, Biolegend #100222) and IgKappa (anti-IgKappa-PE, Biolegend #409506) for 30 min at 4 °C. Cells were then washed and analyzed using flow cytometry. Gating strategy for disease monitoring was identical to that which we reported previously[48] (Supp Fig. 3a in that work). Body weight and body scoring were monitored weekly, and if body weight was reduced by 10%, body weight was monitored daily. Body weight loss equal to 15% and body scoring equal to 2 were considered endpoints for euthanasia. All animals, including mice that did not present signs of disease or morbidity, were euthanized by 24 months.

Immunohistochemistry and pathology. Murine tissues were fixed in 10% buffered neutral formalin overnight, after which bone marrow tissue was decalcified in RapidCal Immuno Buffer (Statlab) for 2 h as previously described[69]. Fixed tissue was then paraffin-embedded and sectioned into 4 μm for immunohistochemistry (IHC) staining. Hematoxylin and eosin (H&E), CD5/PAX5 (CD5 = 1:300 dilution from Sino Biological; PAX5 = 1:100 dilution from Cell Signaling Technology AB_2798001), Ki67 (1:800, Cell Signaling Technology AB_2620142), BCL6 (1:1000, Sigma), MYC (1:1000, Abcam RRID: AB_731658) and IRF4 (1:1000, Cell Signaling Technology AB_62834) staining was performed using standard procedures. Spleen, bone marrow and liver from diseased mice were evaluated by a board-certified pathologist and analysis and classification of leukemia, lymphoma and DLBCL were done following published criteria[124]. CLL cases were characterized by expansion of small PAX5/CD5 double-positive cells with relatively low proliferation rates (Ki-67^{low}), predominantly adjacent to T-cell areas in the spleen and small focal infiltrates in other organs, resembling human CLL. DLBCL/RS cases revealed effacement of spleen, bone marrow and liver architecture by diffuse proliferation of large PAX5/CD5$^{med/low}$/BCL6^{neg}/IRF4+ cells with high proliferation rates (Ki-67^{high}) resembling human DLBCL and RS. Human tissue samples were processed according to CLIA-approved protocols from the Brigham and Women's Hospital pathology department.

BCR-IGHV sequencing. Genomic DNA was isolated from peripheral blood of diseased mice using the QIAGEN DNeasy Blood & Tissue Kit (Qiagen) and analyzed using the mouse-IGH immunoSEQ Assay (Adaptive Biotechnologies). B cell receptor repertoire sequencing was performed using the immunoSEQ Analyzer 3.0 and analyzed using the IMGT/Vquest software to define V, D, J and CDR3 sequences. Mutation status was defined as unmutated when ≥98% homology to the germline was detected.

B-cell purification. Mice were euthanized in a CO_2 chamber, and spleens or femurs were collected and mechanically dissociated to form a single cell suspension. Erythrocyte lysis was performed using ACK buffer and B cells were negatively selected using the MACS Mouse B cell Isolation Kit (Miltenyi Biotec, #130-090-862). B cell purity (>90%) was confirmed post-sorting on a FACS Canto I flow cytometer.

Ex vivo culture of murine primary B cells, drug treatment and BCR stimulation. Ex vivo induction of B-cell proliferation was undertaken using LPS as the mitogenic stimulus, in the presence of IL-4. Purified B cells were seeded at a density of 0.5–0.8 × 10^6/mL and cultured in RPMI/10% FBS containing LPS (50 μg/mL; Sigma, #L6511), murine IL-4 (10 ng/mL; R&D Systems, #404ML010) and β-mercaptoethanol (1:500,000; ThermoFischer Scientific, #21985023) prior to downstream functional studies. Ex vivo B-cell cultures were carried out in the presence or absence of the antioxidant N-acetylcysteine (NAC; 10 mM; Sigma, #A7250), with NAC being replenished every 24 h during the 72-h culture period. For the assessment of sensitivity to parthenolide, B cells were pre-stimulated for 1–2 days with LPS/IL-4 prior to treatment with doubling dilutions of parthenolide (Selleck # S2341) for a further 1–2 days. For the evaluation of DNA damage response, B cells were pre-stimulated with LPS/IL-4 for 2 days prior to treatment with IR (6 Gy) or HU (1 mM; Sigma, #H8627) and incubated for 1, 6, 12 or 24 h, after which the cells were harvested for analysis. For BCR signaling studies, purified splenic B cells (5 × 10^6) were stimulated with 10 μg/mL goat anti-mouse F(ab')2 IgM antibody (Southern Biotech, Birmingham, AL, Cat #1023-01) for 5 or 15 min at 37 °C prior to analysis.

Western blot. Western immunoblot analyses were performed to evaluate the protein expression levels of RPS15 and RPL5, to analyze DNA damage response and BCR signaling, and to validate findings from the Ribo-seq analysis. For all assays, a minimum of 5 × 10^6 cells were collected, washed with PBS and lysed in RIPA buffer (Sigma #R0278) supplemented with protease and phosphatase inhibitors (Sigma #11836153001 and Sigma #4906845001) for 30 min at 4 °C. Cell lysate was clarified by centrifugation at 10,000 × *g* for 5 min. Protein concentration was determined using the Pierce bicinchoninic acid assay (Life Technologies #23225) and 40 μg of protein were loaded per lane on a 4–12% Bis-Tris or 3–8% Tris-Acetate gel (Life Technologies #NP0323 and #EA03785).

Proteins were transferred onto polyvinylidene fluoride membranes (Life Technologies IB24002) using an iBlot 2 at 20 V for 6–12 minutes and subsequently incubated in 5% BSA, 1X TBST (Teknova #T9511) prior to probing with one of the following primary antibodies: RPS15 (1:1000 dilution; #PIPA562977, Thermo Fisher Scientific), RPL5 (1:1000; #14568S, Cell Signaling Technology), ATM (1:1000; #2873, clone D2E2, Cell Signaling Technology), p-ATM Ser1981 (1:250; #AF1655, R&D), SMC1 (1:1000; #4802, Cell Signaling Technology), p-SMC1 Ser957 (1:1000; #4805, clone 5D11G5, Cell Signaling Technology), Chk2 (1:1000; #sc-5278, clone A-12, Santa Cruz), p-Chk2 Thr68 (1:500; #2661, Cell Signaling Technology), Chk1 (1:1000; #sc-8408, clone G-4, Santa Cruz), p-Chk1 Ser345 (1:500; #2341, Cell Signaling Technology), γH2AX Ser139 (1:1000; #05-636, clone JBW301, Millipore; and 1:1000; #2577, Cell Signaling Technology), p53 (1:1000; #9282 and #2524 [clone 1C12], Cell Signaling Technology), p21 (1:500; #64016, Cell Signaling Technology), cyclin A (1:200, #sc-239, clone BF683, Santa Cruz), AKT (1:1000, #4298, clone 40D4, Cell Signaling Technology), p-AKT Ser473 (1:1000, #4060, clone D9E, Cell Signaling Technology), ERK1/2 (1:1000, #4695, clone 137F5, Cell Signaling Technology), p-ERK1/2 Tyr202/204 (1:1000, #4370, clone D13.4.4E, Cell Signaling Technology), p-SYK Tyr525/526 (1:1000, #2711, Cell Signaling Technology), SYK (1:1000, #13198, clone D3Z1E, Cell Signaling Technology), p-PLCγ1 Tyr783 (1:1000, #2821, Cell Signaling Technology), PLCγ1 (1:1000, #5690, clone D9H10, Cell Signaling Technology), GPX1 (1:200; #AF3798, R&D), EIF1AD (1:500, #20528-1, Proteintech), OTUD4 (1:500; #25070-1, Proteintech), PTP4A2 (1:500, #PA5120349, ThermoFisher Scientific), actin (1:2000; #5125, clone 13E5, Cell Signaling Technology), HSP90 (1:1000; #79641, clone C45G5, Cell Signaling Technology) and GAPDH (1:1000; #2118, clone 14C10, Cell Signaling Technology). Membranes were washed in TBST prior to incubation with a 1:2000 or 1:10,000 dilution of goat anti-rabbit HRP-conjugated IgG antibody (Fisher Scientific 12348MI or Cell Signaling Technology, #7074), a 1:1000 dilution of horse anti-mouse HRP-conjugated IgG antibody (Cell Signaling Technology, #7076), or a 1:1000 dilution of rabbit anti-goat HRP-conjugated IgG antibody (R&D, #HAF017) for 1 h at room temperature. Membranes were visualized using SuperSignal West Pico Chemiluminescent Substrate (Life Technologies 34580) and quantified using the BioRad ChemiDoc imaging system. Densitometric quantification of protein bands was carried out using the ImageJ software.

Proliferation assays. Ex vivo proliferation of murine splenic B cells was assessed using the CellTrace Violet Cell Proliferation Kit (ThermoFisher Scientific, #C34557). B cells were resuspended in PBS at 0.8×10^6/mL and incubated at room temperature for 20 min with CellTrace Violet at a final concentration of 10 μM, after which an excess of RPMI/10% FBS was added to stop the reaction. Cells were subsequently cultured in RPMI/10% FBS with LPS/IL-4 for 3 days, harvested and acquired on a LSR Fortessa flow cytometer. Proliferation in the HG3 cell line was measured by plating HG3 cells on 0.01% poly-ornithine-coated plates (Sigma Aldrich #P4957). Cells were imaged every 2 h for the length of time indicated using an IncuCyte S3 Live-Cell Analysis System (Essen Bioscience). Percent confluence was determined by dividing red fluorescence area by total phase cell area, and the assay was conducted in triplicates.

Measurement of apoptosis and cell viability. Apoptotic murine B cells were identified by flow cytometry using the Annexin V Apoptosis Detection Kit with PI (Biolegend, #640914). Cells were washed twice with PBS/0.5%BSA, resuspended in Annexin V binding buffer at a concentration of 5×10^6/mL, stained with FITC-conjugated Annexin V antibody (1:20 dilution) and PI (1:10 dilution) for 15 min at room temperature, and acquired on a LSR Fortessa flow cytometer. Viable cells (Annexin V− PI−) were distinguished from early apoptotic (Annexin V + PI−) and late apoptotic (Annexin V+PI+) cells. Assessment of ex vivo B cell sensitivity to parthenolide was carried out by flow cytometry using the Zombie Violet fixable viability kit (Biolegend, #423114). Cells were washed in PBS and incubated with the Zombie Violet dye (1:1000 dilution in PBS) at 5×10^6 cells/mL for 15 min at room temperature, and acquired on a LSR Fortessa flow cytometer. The surviving fraction corresponding to each drug dose was calculated. The dose-response data were modeled by non-linear regression, and the half maximal effective drug concentration (EC_{50}) was determined using GraphPad Prism v10.0.3.

Cell cycle analysis. Harvested B cells were fixed and permeabilized in ice-cold 80% ethanol and stored overnight at −20 °C. Cells were subsequently washed in PBS and resuspended in PI (20 μg/mL; Sigma, #P4864) and RNase A (1 mg/mL; Invitrogen, #12091021), incubated in darkness at room temperature for 15 min prior to acquisition on a LSR Fortessa flow cytometer. Following the exclusion of doublets and cellular debris, the events were displayed on a PI histogram for analysis. PI binds to cellular DNA and, therefore, measurement of its level reflects the status of a cell within the cell cycle (i.e., G0/G1 phase: 2N; S phase: 2N-4N; G2/M phase: 4 N). A minimum of 100,000 events were analyzed, and experiments were performed in triplicates.

Mitochondrial ROS assay. Quantification of mitochondrial ROS was carried out by flow cytometry using the MitoSOX Red mitochondrial superoxide indicator (Invitrogen, #M36008). Harvested B cells were washed in PBS and resuspended at 5×10^6 cells/mL in pre-warmed MitoSOX staining solution (1 μM MitoSOX Red in PBS), incubated for 30 min at 37 °C in darkness, and acquired on a LSR Fortessa flow cytometer. All experiments were conducted in triplicate and incorporated both a DMSO control and a positive control. Positive control B cells were pretreated with antimycin A (50 μg/mL; Sigma, #A8674) for 2 h at 37 °C prior to analysis with MitoSOX Red.

B cell development. Proportions of murine B cell sub-populations at different development stages were determined by flow cytometric analysis of cell surface markers. Cells were extracted from bone marrow, spleen and the peritoneal cavity and processed as described above (B cell purification). Following dissociation and erythrocyte lysis, cells were washed with PBS supplemented with 2% FCS and 2 mM EDTA and incubated with the following cocktails of antibodies (all purchased from BioLegend) at 1:1000 dilution for 15 min at 4 °C.

Cocktail for splenocyte suspension. CD21-BV421 (Clone 7E9, Cat #123421), B220-BV510 (Clone RA3-6B2, Cat #103247), CD93-BV650 (Clone AA4.1, Cat #136517), CD23-BV786 (Clone B3B34, Cat #563988), CD38-Alexa647 (Clone HIT2, Cat #303514), CD24-Alexa700 (Clone M1/69, Cat #101835), CD95-PE (Clone DX2, Cat #305607), IgD-APC.Cy7 (Clone 11-26 c.2a, Cat #405715), and anti-IgM-PE.Cy7 (Clone MHM-88, Cat #314531; for marginal zone B cells, follicular B cells and transitional B cells quantification).

Cocktail for bone marrow suspension. CD43-PE (Clone S11, Cat# 143205), CD23-BV786 (Clone B3B34, Cat #563988), CD24-Alexa700 (Clone M1/69, Cat #101835), CD93-BV650 (Clone AA4.1, Cat #136517), B220-BV421 (Clone RA3-6B2, Cat #103239), CD11b-PerCP.C5.5 (Clone M1/70, Cat #101227), TER-119-PerCP.C5.5 (Clone TER-119, Cat #116227), CD3e PerCP.C5.5 (Clone KT3.1.1, Cat #155615), Ly6G/Ly6C PerCP.C5.5 (Clone RB6-8C5, Cat #108427), IgD-APC.Cy7 (Clone 11-26.c.2a, Cat #405715) and IgM-PE.Cy7 (Clone MHM-88, Cat #314531; for pro-B cells, pre-B cells, immature, transitional and mature B cells quantification).

Cocktail for peritoneal cavity suspension. CD5-APC (Clone 53-7.3, Cat #100625), B220-BV421 (Clone RA3-6B2, Cat #103239), CD43-PE (Clone S11, Cat #143205), IgM-PE.Cy7 (Clone RMM-1, Cat #406513) and CD23-BV786 (Clone B3B34, Cat #563988; for B1a cells quantification).

Culture of cell lines. HG3 cells (purchased from DSMZ #ACC 765) were cultured in RPMI 1640 (Gibco #11875-093) with 15% fetal bovine serum (FBS) (Sigma-Aldrich), 1% GlutaMAX (Gibco, cat# 35050-061) and 1% penicillin–streptomycin (Life Technologies). Cells were incubated at 37 °C, 5% CO_2 and passaged every 48 h. All subsets of the HG3 cell line were also cultured under these conditions. Cells were routinely tested for mycoplasma per the manufacturer's instructions (VenorGeM Mycoplasma Detection Kit; Sigma-Aldrich #MP0025).

Generation of mutant human CLL cell lines. Sleeping Beauty transposon plasmids carrying one of four *RPS15* CLL mutations (G134R or c.400G>C; H137Y or c.409C>T; S138F or c.413C>T; and S139F or c.416C>T) or the *RPS15* WT gene were assembled by introducing gBlocks® (IDT) containing a Flag and HA tag upstream of the RPS15 WT or mutant coding sequence (codon optimized using the IDT Codon Optimization Tool), with SfiI overhangs on each end. Cloning was performed by digesting both the Sleeping Beauty inducible transposon plasmid pSBtet-GP (Addgene plasmid #60495; contains GFP and puromycin selection markers)[125] and each gBlock with SfiI (#R0123S, New England Biolabs). To generate *RPS15* mutant HG3 cell lines, HG3 cells were electroporated with 15 μg of pCMV(CAT)T7-SB100 (transposase, Addgene #34879) and 15 μg of each of the mutant transposon vectors. Successfully transposed cells were purified twice by FACS post-nucleofection.

To generate cells compatible with the CRISPR-Cas9 system, lentivirus was generated by co-transfection of LentiCas9-Blast (Addgene #52962)[126] along with pMD2.G (Addgene #12259) and psPAX2 (Addgene #12260) into HEK 293T using Lipofectamine 2000® (Life Technologies). Supernatant containing lentiviral particles was collected at 48 and 72 h and concentrated using Lenti-X (Clontech). HG3 cells were transduced with fresh lentivirus in the presence of 8 μg/mL polybrene and selected by blasticidine (20 μg/ml) for 2 weeks and Cas9 activity was tested using a previously reported system[127]. We generated *TP53* knockout HG3 cell lines as previously described[128]. sgRNAs were designed using the online CRISPR design tool (http://crispr.mit.edu/) to target *TP53*. The selection of the sgRNAs was based on choosing those of highest efficiency to target the gene of interest and with the lowest predicted off-targets effects. The sgRNA targeting *TP53* (5′-CCATTGTTCAATATCGTCCG-3′) was cloned into pLKO5.sgRNA.EFS.tRFP (Addgene_#57823). Cloning was carried out as previously described[128] and lentivirus was generated as described above. Cas9-

expressing HG3 cells were transduced with the above *TP53*-targeting construct and RFP+ cells were flow-sorted as single cells into 96-well plates. To confirm CRISPR editing of the *TP53* loci, gDNA was extracted using the QIAampDNA Micro Kit (Qiagen) following the manufacturer's instructions. PCR was performed using primers flanking the target sites for the sgRNAs (Forward: AGACCTGTGGGAAGCGAAAA; Reverse: GACAGGAAGCCAAAGGGTGA). For screening the loss-of-function mutations, PCR products were purified using High Pure PCR Product Purification Kit (Roche) and resulting indels at the expected locations were confirmed by Sanger sequencing. The efficiency of the sgRNAs was assessed by Tracking of Indels by Decomposition (TIDE) software (https://tide-calculator.nki.nl; Netherlands Cancer Institute). Western blots were performed to confirm loss of p53 expression as described above (Western Blot).

Quantitative PCR. Total gDNA or RNA was extracted from HG3 cells using the DNeasy Blood & Tissue Kit (QIAGEN) and the RNA purification kit (QIAGEN), respectively. To make cDNA, 2 μg of RNA was reverse-transcribed into cDNA using the SuperscriptII reverse transcription kit (Life Technologies). mRNA or gDNA templates were quantified using the TaqMan Gene Expression Assay probes (Thermo Fisher): *RPS15* (Hs01358643_g1), *GAPDH* (4333764T), and a customized TaqMan probe specific to the codon-optimized *RPS15* transgene (RPS15_PCW, Assay ID #APT2ADZ). Quantitative real-time PCR was performed on a QuantStudio 6 Flex Real-Time PCR System (Thermo Fisher). Target gene expression was normalized to the mean Ct values of a housekeeping gene (*GAPDH*). Number of transgene integrations was determined by normalizing to endogenous *RPS15*.

Polysome profiling. Cells were lysed in 500 μL polysome lysis buffer (25 mM HEPES pH 7.5, 5 mM $MgCl_2$, 0.1 M KCl, 2 mM DTT, 1% Triton-X, 0.1 mg/mL cycloheximide) and incubated on ice for 5 min. The lysate was centrifuged at 13,000 RPM at 4 °C for 10 min to pellet nuclei. The supernatant was then loaded on top of a 12 mL 10–50% sucrose gradient (25 mM HEPES pH 7.5, 5 mM $MgCl_2$, 0.1 M KCl, 2 mM DTT, 0.1 mg/mL cycloheximide) and spun in an ultracentrifuge at 35,000 RPM at 4 °C for 2 h. Gradients were fractionated into 13 samples and the RNA absorbance throughout the gradient was monitored with a BioComp 153 gradient station ip (BioComp Instruments, Fredericton, New Brunswick), using an FC-2 Triax flow cell with software v1.53A (BioComp), and fractionated with a Gilson FC203B fraction collector.

Sucrose gradients. Cell pellets were lysed in 200 μL lysis buffer (50 mM Hepes pH 7.5, 100 mM KOac, 5 mM $Mg(OAc)_2$, 0.02% digitonin, 1 mM DTT, and 1× cOmplete protease inhibitor cocktail (Roche 1187358)) for 10 min on ice and clarified by centrifugation at 21,130 *g* for 10 minutes at 4 °C. Lysate was normalized to 6 mg/mL based on A_{280} readings prior to loading on a 200 μL 10–50% sucrose gradient. Gradients were spun in a TLS55 rotor (Beckman Coulter) at 259,000 *g* for 30 min at 4 °C with the slowest acceleration and deceleration settings. An input lysate sample and 11 fractions collected from the top of the gradient were directly analyzed by SDS-PAGE and immunoblotting.

Immunofluorescence microscopy. For the quantification of micronuclei, murine B cells were seeded at 10^6 cells/mL in 100 μl PBS onto multispot glass slides that had been pre-coated with poly-L lysine (#P4832, Sigma). Cells were fixed with ice-cold 4% paraformaldehyde for 5 min and nuclear extraction was performed with 10 mM piperazine-N,N′-bis(2-ethanesulfonic acid), 300 mM sucrose, 20 mM sodium chloride, 3 mM magnesium chloride and 0.5% Triton X-100. Following washing in PBS, slides were mounted in Vectashield mounting medium with 4′,6-diamidino-2-phenylindole (DAPI; # H-1200-10, Vector Laboratories), and micronuclei were visualized and enumerated using an ECHO Resolve R4 fluorescence microscope and the ECHO Pro imaging software (Echo Laboratories).

For immunofluorescence analysis of HG3 cells, the cells were cytospun on glass slides at a density of 1×10^6 cells/mL in 200 μL PBS + 10% FCS, fixed in 4% paraformaldehyde at room temperature for 15 min, washed 3 times with PBS + 0.01% TWEEN-20, permeabilized for 5 min in PBS + 0.1% Triton X-100, and blocked for 1 h in PBS + 0.1% TWEEN-20 supplemented with 5% FCS. Cells were incubated overnight at 4 °C with the primary rabbit FLAG antibody (#14793, Cell Signaling Technology). Slides were subsequently washed three times with PBS + 0.1% TWEEN-20, incubated with a secondary anti-rabbit antibody conjugated to Alexa 488 (#ab150077, Abcam) for 1 h at room temperature and washed three times. Nuclei were counterstained with DAPI, and coverslips were mounted using Prolong Gold antifade reagent (#P36934, Life Technologies). Slides were visualized on a Leica SPE confocal microscope. Five fields of view were obtained per condition, and ImageJ software was used for image analysis.

Generation of Ribo-seq Libraries. We obtained ribosome-protected footprints and matching mRNA sequencing data for murine pre-leukemic B cells (3–6 months of age) and HG3 overexpression cell lines (30 μg RNA per sample, 3 biological replicates per condition). RNA-seq libraries were prepared and sequenced as described above. Ribo-seq libraries were generated as previously described[129], with several adaptations. Linkers were designed with 12 random nucleotides forming the UMI rather than 5. RNA unprotected by ribosomes was degraded using a 1:20 dilution of RNaseI and treated for 15 min at room temperature. Ribosomes were isolated using a size-exclusion column as described in the Illumina TruSeq Ribo Profile Kit protocol. Ribosome profiling libraries were sequenced with a single-end 50 bp run on a NextSeq500 (HG3 cells) and with a single-end 75 bp run on a NovaSeq S1 platform (murine B cells).

Ribo-seq analysis. Adapter (AGATCGGAAGAGCACACGTCTGAA) was removed using fastx_clipper from FASTX-Toolkit. UMIs were removed using umi_tools. Ribosomal RNA and tRNA were removed using Bowtie version 1.0.05. For human samples, the remaining reads were aligned to the genome (hg19 / GRCh37) and transcriptome using STAR (v2.5.3a6) (--alignIntronMin 20 --alignIntronMax 100000 --outFilterMismatchNmax 1 --outFilterType BySJout --outFilterMismatchNoverLmax 0.04 --twopassMode Basic). A combination of GENCODE v26lift37 transcriptome annotation was then combined with transcripts annotated as tstatus "unannotated" from MiTranscriptome annotation. To determine the RPF library quality, trinucleotide codon periodicity was plotted using RibORF readDist script8 against annotated protein-coding ORFs (GENCODE v26lift37). Ribo-seq reads were quantified at ORF resolution using a custom script rpfTPM available at https://github.com/TamaraO/Riboseq-tools. Differential translation analysis was performed using DESeq2 and deltaTE [130].

For murine samples, the remaining reads were aligned to the genome (mm10 / GRCm38) and transcriptome using STAR (v2.7.0a) (--alignIntronMin 20 --alignIntronMax 100000 --outFilterMismatchNmax 1 --outFilterType BySJout --outFilterMismatchNoverLmax 0.04 --twopassMode Basic). GENCODE vM24 was parsed for protein-coding regions and the locations of associated stop codons. Trinucleotide codon periodicity was plotted using RibORF readDist script8 against annotated protein-coding ORFs. Ribo-seq reads were further aligned to padded (±20 nucleotides) canonical protein-coding ORFs using STAR (v2.7.0a) (-alignIntronMin 2 --alignIntronMax 1 --outFilterMismatchNmax ---scoreDelOpen −10000 --scoreInsOpen −10000 1 --outFilterType BySJout --outFilterMismatchNoverLmax 0.04 --twopassMode Basic) and quantified at ORF resolution using RSEM (v1.2.31) for compatibility with RNAseq analyses. To determine stop codon readthrough and ribosomal stalling

levels, RPFs ending ± 27 nucleotides around the stop codon were counted using bedtools (v2.29.0). Differential translation efficiency analysis was performed using DESeq2 and the deltaTE.50 protocol. In brief, we use the DESeq2 GLM framework to estimate and test for the significance of the coefficient of the condition:seqtype interaction term, where the coefficient is equivalent to the change in translational efficiency across conditions. To address consistent 3′ bias in the RNAseq data, a second DTE analysis was conducted, considering only RPF and RNAseq read aligning to the 3′-most exons of each gene. Differential ribosomal stalling and stop codon read-through analyses were similarly conducted with DESeq2. To control for readthrough and stalling due to probabilistic molecular errors, GLM model designs were updated to include an interaction term to account for the level of ribosomal occupancy upstream of the stop codon. Given the discovery of widespread readthrough and stalling in preliminary analyses of the models, a custom set of 961 negative control genes (1 > RPF terminating at or past the stop codon across samples) was used instead of the default controls to address the assumption in DESeq2 models that genewise estimates of dispersion are largely unchanged across samples.

Selection of DTE genes for experimental validation. Genes were selected for experimental validation based on whether the gene displayed significant evidence of differential translation across three analyses: differential translation efficiency (DTE), DTE at the 3′ exon, and differential protein expression (based on proteomics data) analysis. To derive an appropriate padj threshold for individual comparative analyses, p-values were confirmed to be uncorrelated across analyses and such that each analysis could be treated as an independent test for differential translation. Thus, a threshold of padj <0.368 was enforced for each comparative analysis to achieve an overall false discovery rate (FDR) of $(0.368)^3 = 0.05$ in the final joint analysis. Genes designated as differentially translated between conditions were also required to have log2 fold changes (log2FC) of the same sign (either "+" or "−") across all three metrics. Of these 29 genes identified, 6 were selected for validation by western blot based on more stringent criteria (DESeq2 Wald test FDR-adjusted $p < 0.25$ across all 3 analyses, | log2FC | > 0.5 in DTE analyses).

Generation of mouse and primary human RNA-sequencing libraries. Murine B cells (1×10^6) were isolated and purified from the spleens of 3–6 month old Rps15 wild-type, heterozygous and homozygous mutant mice (as described above), or from 20 to 24 month old non-leukemia mice. B220 + CD5 + CLL cells were FACS sorted from human primary CLL samples (gating strategy identical to that which we previously reported[116]. Post-isolation, cells were washed in cold PBS and total RNA was extracted using a RNeasy kit (Qiagen). Total RNA was quantified using the Quant-iT RiboGreen RNA Assay Kit and normalized to 5 ng/μL. 2 μL of ERCC controls (using a 1:1000 dilution) were spiked into each sample. For cDNA library preparation, 200 ng per sample was used as input into an automated variant of the Illumina TruSeq Stranded mRNA Sample Preparation Kit (which preserves the strand orientation of the RNA transcript). Oligo dT beads were used to enrich mRNA from the total RNA sample, followed by heat fragmentation and cDNA synthesis. The resultant 400 bp cDNA underwent dual-indexed library preparation, including 'A' base addition, adapter ligation using P7 adapters, and PCR enrichment using P5 adapters. After enrichment, libraries were quantified using Quant-iT PicoGreen (1:200 dilution). Samples were subsequently normalized to 5 ng/μL, pooled and quantified using the KAPA Library Quantification Kit for Illumina Sequencing Platforms. The entire process was performed in a 96-well format and all pipetting was executed by either Agilent Bravo or Hamilton Starlet. Samples underwent single-end sequencing for 75 cycles using an Illumina NextSeq platform.

RNA-sequencing analysis

Patient samples. RNA-sequencing reads were aligned to the human reference genome GrCH38 using STAR (v2.4.0.1)[131] and TPM (Transcripts Per Kilobase Million) values were used to measure gene expression. Differentially expressed genes were determined using DESeq2. Pathway analysis was performed using the MetaCore software (Clarivate Analytics) or GSEA [132].

Human cell lines. RNA-seq reads were aligned with STAR (version 2.5.3a) with the following parameters: --runThreadN 4 --genomeDir /cga/wu/riboseq/reference/STAR_index_RPS15_mCherry --limitBAMsortRAM 30000000000 --outSAMtype BAM SortedByCoordinate --outFilterType BySJout --alignIntronMin 20 --alignIntronMax 100000 --quantMode TranscriptomeSAM --twopassMode Basic. A custom genome was built by adding RPS15 transgene sequences (mutant and wild-type) to the FASTA file of the human genome (hg19). For the transcriptome annotation, a combination of GENCODE v26lift37 transcriptome annotation was combined with transcripts annotated as tstatus "unannotated" from MiTranscriptome annotation[133]. RSEM (v1.3)[63] was used to quantify transcription against the same transcriptome annotation as above. DESeq2 was used to perform differential gene expression analysis.

Mouse samples. RNAseq reads were aligned with STAR as described above, except against the mouse genome GRCm38 and GENCODE annotation of the transcriptome vM24. Quantification was performed with RSEM. Differential gene expression analysis was performed with DESeq2.

RNA-seq libraries of aged, non-leukemic Rps15 heterozygous mice showed significant Clontech SMART CDS Primer II A adapter content. To address this issue, we explicitly trimmed and filtered out reads with cutadapt using the following parameters: -b GCTAATCATTGCAAG CAGTGGT ATCAACGCAGAGTACATT -b AAGCAGTGGTATCAACGCA GAGTACATT -b GGGGGG GGGGGGGGGGGGGGGGGGGGGGGGG GGGGGGGGGGGGGGGG -m 40. Following filtering, the libraries displayed no apparent QC issues; we thus proceeded with analysis as described above.

Mass spectroscopy of protein samples. Murine B cells (30 million cells) were isolated and purified from the spleens of 3–6 month old *Rps15* wild-type, heterozygous and homozygous mutant mice ($n = 3$ mice per genotype). Total protein content was first quantified with Pierce™ micro-BCA assay. Samples were then reduced with DTT and alkylated with iodoacetamide. Proteins were precipitated with a methanol/chloroform solution. Protein pellets were resuspended in 200 mM EPPS, pH 8.0. Protein digestion was performed sequentially using LysC (1:50) and Trypsin (1:100) based on protease to protein ratio. Peptides from each sample were then labeled with a unique tandem mass tag (10 in total) to enable sample multiplexing. To verify successful TMT-labeling, 2 μL of each labeled sample was set aside for checking the relative abundances of TMTs. The single multiplexed sample was then flowed through a basic pH reverse phase fractionation column while gradually increasing buffer ratio over time (Buffer A: 5% ACN, 50 mM Ammonium Bicarbonate pH 8.0 m; Buffer B: Buffer B: 90% ACN, Ammonium Bicarbonate pH 8.0). A total of 24 fractions (100 μL, 37-s windows) were collected from the flow thru. Proteome data were collected on an Orbitrap Eclipse mass spectrometer (ThermoFisher Scientific) coupled to a Proxeon EASY-nLC 1000 LC pump (ThermoFisher Scientific).

Fractionated peptides were separated using a 120 min gradient at 500 nL/min on a 35 cm column (i.d. 100 μm, Accucore, 2.6 μm, 150 Å) packed in-house. MS1 data were collected in the Orbitrap (120,000 resolution; maximum injection time 50 ms; AGC 4×10^5). Charge states between 2 and 5 were required for MS2 analysis, and a 120 s dynamic exclusion window was used. Top 10 MS2 scans were performed in the

ion trap with CID fragmentation (isolation window 0.5 Da; Rapid; NCE 35%; maximum injection time 50 ms; AGC 2×10^4). An on-line real-time search algorithm (Orbiter) was used to trigger MS3 scans for quantification. [PMID: 32126768] MS3 scans were collected in the Orbitrap using a resolution of 50,000, NCE of 45%, maximum injection time of 150 ms, and AGC of 1.5×10^5. The close out was set at two peptides per protein per fraction [PMID: 32126768].

Proteomic analysis. MS2 spectra were analyzed with Proteome Discoverer (v2.5, Thermo Fisher Scientific) using the SEQUEST algorithm against an Uniprot composite database derived from the Mouse proteome containing its reversed complement and known contaminants (Peptide Mass Tolerance=20 ppm, Fragment Ion Tolerance=1, Max Internal Cleavage Site=2, Max differential/Sites = 4, Differential Modification=Methionine Oxidation). Peptide spectral matches were filtered to a 1% false discovery rate (FDR) using the target-decoy strategy combined with linear discriminant analysis. For reporter ion quantification, we ran SEQUEST with the following parameters: mass tolerance = 0.003, ms3 = 1, peak_picking = max, num_isotopes = 2, ms2_isolation_width = 0.5, ms3_isolation_width = 1.2. Thus, proteins were quantified only from peptides with a summed SN threshold of >100 and MS2 isolation specificity of 0.5.

A matrix of summed intensities representing the abundance of each protein across samples was analyzed with DESeq2 to identify differentially expressed proteins. 6582 of 9544 protein-coding genes from the Ribo-seq dataset were also captured in the proteomics dataset (pre-filtering). Since stringent filtering of proteomics results resulted in the loss of a substantive portion of the dataset, we did not use this proteomics data for systematic corroboration of differentially translated genes identified by Ribo-seq analysis, but rather used it to enable prioritization of targets for validation Western blotting experiments, focusing on the most significant DTE genes across analyses.

Generation of mouse whole genome sequencing libraries. Genome sequencing was performed on flow-cytometry-sorted tumor cells from the spleens of four *Rps15*^{Het} mice, two *Trp53*^{del} mice, and two *Rps15*^{Het}/*Trp53*^{del} diseased mice as well as paired T cells as germline control. One microgram of genomic DNA was used for library preparation. Samples underwent acoustic shearing using a Covaris focused ultrasonicator targeting 385-bp fragments, after which size selection was performed using SPRI cleanup. DNA libraries were constructed using the KAPA Library Prep Kit (KAPA Biosystems) using palindromic forked adapters with 8 base unique index sequences (IDT) embedded within the adapter. Libraries were subsequently quantified using PCR with adapter-specific probes (KAPA Biosystems), normalized to 2.2 nmol/L, pooled into 24 plexes, and loaded onto a NovaSeq 6000 S4 flowcell. Cluster amplification and sequencing were performed via sequencing-by-synthesis kits to produce 151-bp paired-end reads.

Whole genome sequencing analysis. Illumina sequencing data were aligned to the GRCm38 reference sequence with bwa version 0.7.15 (134[134]). Aligned reads were then deduplicated and base quality scores were recalibrated with GATK version 4.1.8.1. Somatic SNVs and InDels were detected by the intersection of two callers: Mutect2 (GATK) and Strelka2 ref version 2.9.3. Candidate InDels were first called by Manta version 1.5.0 before being filtered with Strelka2. Functional impacts of mutations were inferred by and annotated with SIFT4. Somatic mutation signatures were generated as previously described[127]. The number of instances of each base-base transitions were counted with respect to their trinucleotide contexts and overrepresented transitions were identified with FDR-corrected hypergeometric tests (q-value < 0.05). The rank of the transition matrix (number of signatures) and over-representation of specific transitions were validated with de novo mutational signature analysis using mutSignatures R package[135]. Copy ratios over chromosomal segments were first computed with a GATK-based pipeline and recurrent somatic copy number alterations were subsequently identified with GISTIC version 2.0.23 (q-value < 0.25). CNV plots were generated using average sample/normal B-cell copy ratio within a running window of 0.1 M base pairs [136,137].

Statistics and reproducibility. Statistical analysis was performed using GraphPad Prism v10.0.3 unless otherwise specified in the Methods. For comparison of 3 or more groups, P-values were calculated using one-way ANOVA followed by Tukey's multiple comparison test. For significantly different standard deviations, p-values were calculated using the Mann-Whitney test. Two-group comparisons were performed using two-sample Student t tests as detailed in each respective figure legend. Survival analyses were conducted using the log-rank test with Bonferroni correction for multiple comparisons. For all of the above, the significance threshold was set at $P \leq 0.05$. No data were excluded from these analyses and the investigators were not blinded to allocation during experiments and outcome assessment. No statistical method was used to predetermine sample size for the individual mouse cohorts.

For differential expression analyses comparing cells of a single lineage from mice under a single experimental condition to those of syngeneic, age-matched controls (paired-sample experiment), three samples per condition are sufficient to achieve power ≥0.8 according to simulation studies and thus a sample size of 3 per condition was selected for all differential expression analyses[138]. Genomic characterization studies with paired tumor-normal samples with tumors sequenced to a depth greater than 50x and to a comparable depth for the matched normal sample are sufficiently sensitive (sensitivity > 0.8) to detect somatic mutations with VAF > 0.10[139]. Thus, a tumor sequencing depth of 60x and a matched normal sequencing depth of 30× were selected for whole genome sequencing analyses.

All experimental replicates represent biological replicates. Unless otherwise stated in the figure legend, three biological replicates of each genotype were used. In all mouse experiments detailed in this manuscript, cohorts were balanced by sex. Mice were either 3–6 months of age or >12 months of age in the experiments detailed above, as noted in the respective text or figure legends.

Reporting summary

Further information on research design is available in the Nature Portfolio Reporting Summary linked to this article.

Data availability

The molecular data used in this study are publicly available and are included in the following patient cohorts (Fig. 1a, Supp Fig. 1a-c, Supp Table 1, Supp Data 1): Dana-Farber Cancer Institute (DFCI), German CLL Study Group (GCLLSG), French CLL Cohort, International Cancer Genome Consortium (ICGC), MD Anderson Cancer Center (MDACC), National Heart Lung and Blood Institute (NHLBI) and University of California San Diego (UCSD). Sequencing, expression, and genotyping is available at European Genome-Phenome Archive (EGA, http://www.ebi.ac.uk/ega/), which is hosted at the European Bioinformatics Institute (EBI), under accession numbers EGAS00000000092 (ICGC cohort) and in dbGaP under accession numbers: phs001473.v2.p1 (MDACC, NHLBI), phs000922.v2.p1 (GCLLSG), phs001431.v2.p1 (DFCI, UCSD), phs001091.v1.p1 (MDACC), phs000435.v3.p1 (DFCI), phs002297.v2.p1 (NHLBI), phs000879.v1.p1 (DFCI), phs002335.v1 (French), and GEO accession number GSE143673 (GCLLSG). All reported RNA-seq and Riboseq data, including raw sequencing and quantitation files, have been deposited to the GEO repository (GSE293841), and can be accessed at https://www.ncbi.nlm.nih.gov/geo/query/acc.cgi?acc=GSE293841. The mass spectrometry proteomics data have been deposited to the ProteomeXchange Consortium via the PRIDE [1] partner repository with the dataset identifier

PXD071901. Source data for all figures are provided as a Source Data file with this paper. Source data are provided with this paper.

Materials availability

The Cd19-Cre/Rps15-S138F flox mouse strain will be available at the Jackson Laboratory Repository with the JAX Stock no. 037632 (http://jaxmice.jax.org/query).

Code availability

Supplementary and wrapper scripts used to conduct genomics, transcriptomics, and ribosomal sequencing analyses are made available via the following links to publicly accessible repositories: GitHub Repository: https://github.com/nruthen/RPS15_Mutant_Mouse_Multiomics. https://doi.org/10.5281/zenodo.17548003. Terra Workspace: https://app.terra.bio/#workspaces/cll-mouse/Wu_RPS15_Catherine_Analysis_Workspace.

References

1. Goudarzi, K. M. & Lindström, M. S. Role of ribosomal protein mutations in tumor development (Review). *Int. J. Oncol.* **48**, 1313–1324 (2016).
2. Keersmaecker, K. D. et al. Exome sequencing identifies mutation in CNOT3 and ribosomal genes RPL5 and RPL10 in T-cell acute lymphoblastic leukemia. *Nat. Genet.* **45**, 186–190 (2013).
3. Lawrence, M. S. et al. Discovery and saturation analysis of cancer genes across 21 tumor types. *Nature*. **505**, 495–501 (2014).
4. Nieminen, T. T. et al. Germline mutation of RPS20, encoding a ribosomal protein, causes predisposition to hereditary nonpolyposis colorectal carcinoma without DNA mismatch repair deficiency. *Gastroenterology*. **147**, 595–598.e5 (2014).
5. Novetsky A. P. et al. Frequent mutations in the RPL22 gene and its clinical and functional implications. *Gynecol Oncol*. 2013;128: https://doi.org/10.1016/j.ygyno.2012.10.026.
6. Hofman, I. J. F. et al. RPL5 on 1p22.1 is recurrently deleted in multiple myeloma and its expression is linked to bortezomib response. *Leukemia*. **31**, 1706–1714 (2017).
7. Fancello, L., Kampen, K. R., Hofman, I. J. F., Verbeeck, J. & De Keersmaecker, K. The ribosomal protein gene RPL5 is a haploinsufficient tumor suppressor in multiple cancer types. *Oncotarget*. **8**, 14462–14478 (2017).
8. Landau, D. A. et al. Mutations driving CLL and their evolution in progression and relapse. *Nature*. **526**, 525–530 (2015).
9. Hernández-Sánchez, M. et al. CLL cells cumulate genetic aberrations prior to the first therapy even in outwardly inactive disease phase. *Leukemia*. **33**, 518–558 (2019).
10. Ljungström, V. et al. Whole-exome sequencing in relapsing chronic lymphocytic leukemia: clinical impact of recurrent RPS15 mutations. *Blood*. **127**, 1007–1016 (2016).
11. Burger, J. A. et al. Clonal evolution in patients with chronic lymphocytic leukaemia developing resistance to BTK inhibition. *Nat. Commun.* **7**, 11589 (2016).
12. Sulima, S. O., Kampen, K. R. & De Keersmaecker, K. Cancer biogenesis in ribosomopathies. *Cells*. **8**, 229 (2019).
13. Sulima, S. O., Hofman, I. J. F., De Keersmaecker, K. & Dinman, J. D. How ribosomes translate cancer. *Cancer Discov.* **7**, 1069–1087 (2017).
14. Bastide, A. & David, A. The ribosome, (slow) beating heart of cancer (stem) cell. *Oncogenesis*. **7**, 34 (2018).
15. Pelletier, J., Thomas, G. & Volarević, S. Ribosome biogenesis in cancer: new players and therapeutic avenues. *Nat. Rev. Cancer*. **18**, 51–63 (2018).
16. Kampen, K. R. et al. The ribosomal RPL10 R98S mutation drives IRES-dependent BCL-2 translation in T-ALL. *Leukemia*. **33**, 319–332 (2019).
17. Kampen, K. R., Sulima, S. O., Vereecke, S. & De Keersmaecker, K. Hallmarks of ribosomopathies. *Nucleic Acids Res.* **48**, 1013–1028 (2020).
18. Sulima, S. O. et al. Ribosomal lesions promote oncogenic mutagenesis. *Cancer Res.* **79**, 320–327 (2019).
19. De Keersmaecker, K., Sulima, S. O. & Dinman, J. D. Ribosomopathies and the paradox of cellular hypo- to hyperproliferation. *Blood*. **125**, 1377–1382 (2015).
20. Sulima, S. O. et al. Bypass of the pre-60S ribosomal quality control as a pathway to oncogenesis. *Proc. Natl. Acad. Sci. Proc. Natl. Acad. Sci.* **111**, 5640–5645 (2014).
21. Ajore, R. et al. Deletion of ribosomal protein genes is a common vulnerability in human cancer, especially in concert with TP53 mutations. *EMBO Mol. Med.* **9**, 498–507 (2017).
22. Zhang, Y. & Lu, H. Signaling to p53: ribosomal proteins find their way. *Cancer Cell*. **16**, 369–377 (2009).
23. Golomb, L., Volarevic, S. & Oren, M. p53 and ribosome biogenesis stress: the essentials. *FEBS Lett.* **588**, 2571–2579 (2014).
24. Liu, Y., Deisenroth, C. & Zhang, Y. RP–MDM2–p53 pathway: linking ribosomal biogenesis and tumor surveillance. *Trends Cancer*. **2**, 191–204 (2016).
25. Deisenroth, C. & Zhang, Y. Ribosome biogenesis surveillance: probing the ribosomal protein-Mdm2-p53 pathway. *Oncogene*. **29**, 4253–4260 (2010).
26. Marechal, V., Elenbaas, B., Piette, J., Nicolas, J. C. & Levine, A. J. The ribosomal L5 protein is associated with mdm-2 and mdm-2-p53 complexes. *Mol. Cell Biol.* **14**, 7414–7420 (1994).
27. Zhang, Y. et al. Ribosomal protein L11 negatively regulates oncoprotein MDM2 and mediates a p53-dependent ribosomal-stress checkpoint pathway. *Mol. Cell Biol.* **23**, 8902–8912 (2003).
28. Dai, M.-S. et al. Ribosomal protein L23 activates p53 by inhibiting MDM2 function in response to ribosomal perturbation but not to translation inhibition. *Mol. Cell Biol.* **24**, 7654–7668 (2004).
29. Chen, D. et al. Ribosomal protein S7 as a novel modulator of p53-MDM2 interaction: binding to MDM2, stabilization of p53 protein, and activation of p53 function. *Oncogene*. **26**, 5029–5037 (2007).
30. Daftuar, L., Zhu, Y., Jacq, X. & Prives, C. Ribosomal proteins RPL37, RPS15 and RPS20 regulate the Mdm2-p53-MdmX network. *PLoS One*. **8**, e68667 (2013).
31. Dameshek, W. Riddle: What do aplastic anemia, paroxysmal nocturnal hemoglobinuria (PNH) and "hypoplastic": leukemia have in common? *Blood*. **30**, 251–254 (1967).
32. Kang, J. et al. Ribosomal proteins and human diseases: molecular mechanisms and targeted therapy. *Sig Transduct. Target Ther.* **6**, 1–22 (2021).
33. Kapralova, K. et al. Oxidative DNA damage, inflammatory signature, and altered erythrocytes properties in diamond-blackfan anemia. *Int. J. Mol. Sci.* **21**, 9652 (2020).
34. Bretones, G. et al. Altered patterns of global protein synthesis and translational fidelity in RPS15-mutated chronic lymphocytic leukemia. *Blood*. **132**, 2375–2388 (2018).
35. Ntoufa, S. et al. RPS15 mutations rewire RNA translation in chronic lymphocytic leukemia. *Blood Adv.* **5**, 2788–2792 (2021).
36. Knisbacher B. A. et al. Molecular map of chronic lymphocytic leukemia and its impact on outcome. *Nat. Genet.* (2022)
37. Rössler, I. et al. The C-terminal tail of ribosomal protein Rps15 is engaged in cytoplasmic pre-40S maturation. *RNA Biol.* **19**, 560–574 (2022).
38. Yu, L. et al. Survival of Del17p CLL depends on genomic complexity and somatic mutation. *Clin. Cancer Res.* **23**, 735–745 (2017).
39. Kwok, M., Agathanggelou, A. & Stankovic, T. DNA damage response defects in hematologic malignancies: mechanistic insights and therapeutic strategies. *Blood*. **143**, 2123–2144 (2024).

40. Wang, D.-M. et al. Intermediate prognosis of 6q deletion in chronic lymphocytic leukemia. *Leuk. Lymphoma*. **52**, 230–237 (2011).
41. Lipreri da Silva, J. C. et al. Ezrin is highly expressed and a druggable target in chronic lymphocytic leukemia. *Life Sci.* **311**, 121146 (2022).
42. Song, Y. et al. Ezrin mediates invasion and metastasis in tumorigenesis: a review. *Front. Cell Dev. Biol.* **8**, 588801 (2020).
43. Li, X., Jin, F. & Li, Y. A novel autophagy-related lncRNA prognostic risk model for breast cancer. *J. Cell Mol. Med.* **25**, 4–14 (2021).
44. Khan, T., Kryza, T., Lyons, N. J., He, Y. & Hooper, J. D. The CDCP1 signaling hub: a target for cancer detection and therapeutic intervention. *Cancer Res.* **81**, 2259–2269 (2021).
45. Yang, G. et al. circ-BIRC6, a circular RNA, promotes hepatocellular carcinoma progression by targeting the miR-3918/Bcl2 axis. *Cell Cycle*. **18**, 976–989 (2019).
46. Han, Y. & Wang, H. MiR-3918 inhibits tumorigenesis of glioma via targeting EGFR to regulate PI3K/AKT and ERK pathways. *J. Mol. Neurosci.* **72**, 433–440 (2022).
47. Klintman, J. et al. Genomic and transcriptomic correlates of Richter transformation in chronic lymphocytic leukemia. *Blood*. **137**, 2800–2816 (2021).
48. Moulin, C. et al. Clinical, biological, and molecular genetic features of Richter syndrome and prognostic significance: a study of the French Innovative Leukemia Organization. *Am. J. Hematol.* **96**, E311–E314 (2021).
49. Nadeu F. et al. Detection of early seeding of Richter transformation in chronic lymphocytic leukemia. *Nat Med.* 1–10 (2022).
50. Steele, A. J. et al. The sesquiterpene lactone parthenolide induces selective apoptosis of B-chronic lymphocytic leukemia cells in vitro. *Leukemia*. **20**, 1073–1079 (2006).
51. Li, X. et al. Derivatisation of parthenolide to address chemoresistant chronic lymphocytic leukaemia. *Medchemcomm*. **10**, 1379–1390 (2019).
52. Agathanggelou, A. et al. Targeting the Ataxia Telangiectasia mutated-null phenotype in chronic lymphocytic leukemia with pro-oxidants. *Haematologica*. **100**, 1076–1085 (2015).
53. Akasaka, S. & Yamamoto, K. Hydrogen peroxide induces G:C to TA and G:C to C:G transversions in the supF gene of *Escherichia coli*. *Mol. Gen. Genet*. **243**, 500–505 (1994).
54. Lee, D., O'Connor, T. R. & Pfeifer, G. P. Oxidative DNA damage induced by copper and hydrogen peroxide promotes CG→TT tandem mutations at methylated CpG dinucleotides in nucleotide excision repair-deficient cells. *Nucleic Acids Res.* **30**, 3566–3573 (2002).
55. el-Deiry, W. S. et al. WAF1/CIP1 is induced in p53-mediated G1 arrest and apoptosis. *Cancer Res.* **54**, 1169–1174 (1994).
56. Harper, J. W., Adami, G. R., Wei, N., Keyomarsi, K. & Elledge, S. J. The p21 Cdk-interacting protein Cip1 is a potent inhibitor of G1 cyclin-dependent kinases. *Cell*. **75**, 805–816 (1993).
57. Deng, C., Zhang, P., Harper, J. W., Elledge, S. J. & Leder, P. Mice lacking p21CIP1/WAF1 undergo normal development, but are defective in G1 checkpoint control. *Cell*. **82**, 675–684 (1995).
58. Karanjawala, Z. E., Murphy, N., Hinton, D. R., Hsieh, C. L. & Lieber, M. R. Oxygen metabolism causes chromosome breaks and is associated with the neuronal apoptosis observed in DNA double-strand break repair mutants. *Curr. Biol.* **12**, 397–402 (2002).
59. Sallmyr, A., Fan, J. & Rassool, F. V. Genomic instability in myeloid malignancies: increased reactive oxygen species (ROS), DNA double strand breaks (DSBs) and error-prone repair. *Cancer Lett.* **270**, 1–9 (2008).
60. Tanaka, T., Halicka, H. D., Huang, X., Traganos, F. & Darzynkiewicz, Z. Constitutive histone H2AX phosphorylation and ATM activation, the reporters of DNA damage by endogenous oxidants. *Cell Cycle*. **5**, 1940–1945 (2006).
61. Letavayová, L. et al. Relative contribution of homologous recombination and non-homologous end-joining to DNA double-strand break repair after oxidative stress in Saccharomyces cerevisiae. *DNA Repair*. **5**, 602–610 (2006).
62. Sharma, V. et al. Oxidative stress at low levels can induce clustered DNA lesions leading to NHEJ-mediated mutations. *Oncotarget*. **7**, 25377–25390 (2016).
63. Lee, T., Yao, G., Nevins, J. & You, L. Sensing and integration of Erk and PI3K signals by Myc. *PLoS Comput. Biol.* **4**, e1000013 (2008).
64. Tsai, W.-B. et al. Activation of RAS/PI3K/ERK pathway induces c-Myc stabilization to upregulate argininosuccinate synthetase, leading to arginine deiminase resistance in melanoma cells. *Cancer Res.* **72**, 2622–2633 (2012).
65. Chen, J. et al. ZAP-70 constitutively regulates gene expression and protein synthesis in chronic lymphocytic leukemia. *Blood*. **137**, 3629–3640 (2021).
66. Chen, J., Moore, A. & Ringshausen, I. ZAP-70 shapes the immune microenvironment in B cell malignancies. *Front. Oncol.* **10**, 595832 (2020).
67. Adams, D. J. et al. Genetic determinants of micronucleus formation in vivo. *Nature*. **627**, 130–136 (2024).
68. Hosea, R., Hillary, S., Naqvi, S., Wu, S. & Kasim, V. The two sides of chromosomal instability: drivers and brakes in cancer. *Signal Transduct. Target. Ther.* **9**, 75 (2024).
69. Biran, A. et al. Activation of notch and Myc signaling via B-cell-restricted depletion of Dnmt3a generates a consistent murine model of chronic lymphocytic leukemia. *Cancer Res.* **81**, 6117–6130 (2021).
70. Chang, A. et al. Recruitment of KMT2C/MLL3 to DNA damage sites mediates DNA damage responses and regulates PARP inhibitor sensitivity in cancer. *Cancer Res.* **81**, 3358–3373 (2021).
71. Lv, S. et al. Loss of KMT2D induces prostate cancer ROS-mediated DNA damage by suppressing the enhancer activity and DNA binding of antioxidant transcription factor FOXO3. *Epigenetics*. **14**, 1194–1208 (2019).
72. Sun, L. et al. MGA mutation as a novel biomarker for immune checkpoint therapies in non-squamous non-small cell lung cancer. *Front. Pharm.* **12**, 625593 (2021).
73. Llabata, P. et al. MAX mutant small-cell lung cancers exhibit impaired activities of MGA-dependent noncanonical polycomb repressive complex. *Proc. Natl. Acad. Sci. USA*. **118**, e2024824118 (2021).
74. Chan, D. K. H. et al. Biallelic FBXW7 knockout induces AKAP8-mediated DNA damage in neighbouring wildtype cells. *Cell Death Discov.* **9**, 1–15 (2023).
75. Lan, H. & Sun, Y. Tumor suppressor FBXW7 and its regulation of DNA damage response and repair. *Front Cell Dev. Biol.* **9**, 751574 (2021).
76. Close, V. et al. FBXW7 mutations reduce binding of NOTCH1, leading to cleaved NOTCH1 accumulation and target gene activation in CLL. *Blood*. **133**, 830–839 (2019).
77. Llabata, P. et al. Multi-omics analysis identifies MGA as a negative regulator of the MYC pathway in lung adenocarcinoma. *Mol. Cancer Res.* **18**, 574–584 (2020).
78. Mathsyaraja H. et al. Loss of MGA repression mediated by an atypical polycomb complex promotes tumor progression and invasiveness. eLife. **10**:e64212 (2021).
79. Chitalia, A. et al. Descriptive analysis of genetic aberrations and cell of origin in Richter transformation. *Leuk. Lymphoma*. **60**, 971–979 (2019).
80. Parry, E. M. et al. Evolutionary history of transformation from chronic lymphocytic leukemia to Richter syndrome. *Nat. Med.* **29**, 158–169 (2023).
81. Léger-Silvestre, I. et al. Specific role for yeast homologs of the Diamond Blackfan Anemia-associated Rps19 protein in ribosome synthesis. *J. Biol. Chem.* **280**, 38177–38185 (2005).
82. Léger-Silvestre, I. et al. The ribosomal protein Rps15p is required for nuclear exit of the 40S subunit precursors in yeast. *EMBO J.* **23**, 2336–2347 (2004).

83. Ferreira-Cerca, S., Pöll, G., Gleizes, P.-E., Tschochner, H. & Milkereit, P. Roles of eukaryotic ribosomal proteins in maturation and transport of pre-18S rRNA and ribosome function. *Mol. Cell*. **20**, 263–275 (2005).
84. Khairulina, J. et al. Eukaryote-specific motif of ribosomal protein S15 neighbors A site codon during elongation and termination of translation. *Biochimie*. **92**, 820–825 (2010).
85. Bulygin, K., Chavatte, L., Frolova, L., Karpova, G. & Favre, A. The first position of a codon placed in the A site of the human 80S ribosome contacts nucleotide C1696 of the 18S rRNA as well as proteins S2, S3, S3a, S30, and S15. *Biochemistry*. **44**, 2153–2162 (2005).
86. Pisarev, A. V. et al. Specific functional interactions of nucleotides at key −3 and +4 positions flanking the initiation codon with components of the mammalian 48S translation initiation complex. *Genes Dev.* **20**, 624–636 (2006).
87. Robinson, J. T., Thorvaldsdóttir, H., Wenger, A. M., Zehir, A. & Mesirov, J. P. Variant review with the integrative genomics viewer. *Cancer Res.* **77**, e31–e34 (2017).
88. Handy, D. E. et al. Glutathione peroxidase-1 regulates mitochondrial function to modulate redox-dependent cellular responses. *J. Biol. Chem.* **284**, 11913–11921 (2009).
89. Zhao, Y. et al. Noncanonical regulation of alkylation damage resistance by the OTUD4 deubiquitinase. *EMBO J.* **34**, 1687–1703 (2015).
90. Chai, B., Huang, J., Cairns, B. R. & Laurent, B. C. Distinct roles for the RSC and Swi/Snf ATP-dependent chromatin remodelers in DNA double-strand break repair. *Genes Dev.* **19**, 1656–1661 (2005).
91. Park, J.-H. et al. Mammalian SWI/SNF complexes facilitate DNA double-strand break repair by promoting gamma-H2AX induction. *EMBO J.* **25**, 3986–3997 (2006).
92. Ogiwara, H. et al. Histone acetylation by CBP and p300 at double-strand break sites facilitates SWI/SNF chromatin remodeling and the recruitment of non-homologous end joining factors. *Oncogene*. **30**, 2135–2146 (2011).
93. Lee, H.-S., Park, J.-H., Kim, S.-J., Kwon, S.-J. & Kwon, J. A cooperative activation loop among SWI/SNF, γ-H2AX and H3 acetylation for DNA double-strand break repair. *EMBO J.* **29**, 1434–1445 (2010).
94. Peng, G. et al. BRIT1/MCPH1 links chromatin remodelling to DNA damage response. *Nat. Cell Biol.* **11**, 865–872 (2009).
95. Pace, P. et al. FANCE: the link between Fanconi anaemia complex assembly and activity. *EMBO J.* **21**, 3414–3423 (2002).
96. Wang, X. et al. Chk1-mediated phosphorylation of FANCE is required for the Fanconi anemia/BRCA pathway. *Mol. Cell Biol.* **27**, 3098–3108 (2007).
97. Sunavala-Dossabhoy, G. & De Benedetti, A. Tousled homolog, TLK1, binds and phosphorylates Rad9; TLK1 acts as a molecular chaperone in DNA repair. *DNA Repair*. **8**, 87–102 (2009).
98. TLK1B promotes repair of DSBs via its interaction with Rad9 and Asf1 Caroline Canfield, justin rains, and Arrigo De Benedetti - PMC [Internet]. [cited 7 Nov 2023]. Available from: https://www.ncbi.nlm.nih.gov/pmc/articles/PMC2803485/
99. Werner, S. R. et al. Enhanced cell cycle progression and down regulation of p21(Cip1/Waf1) by PRL tyrosine phosphatases. *Cancer Lett.* **202**, 201–211 (2003).
100. Lunardi, A. et al. A genome-scale protein interaction profile of Drosophila p53 uncovers additional nodes of the human p53 network. *Proc. Natl. Acad. Sci. USA*. **107**, 6322–6327 (2010).
101. Tompkins, V. S. et al. A novel nuclear interactor of ARF and MDM2 (NIAM) that maintains chromosomal stability. *J. Biol. Chem.* **282**, 1322–1333 (2007).
102. Annibaldis, G. et al. Readthrough of stop codons under limiting ABCE1 concentration involves frameshifting and inhibits nonsense-mediated mRNA decay. *Nucleic Acids Res.* **48**, 10259–10279 (2020).
103. Mangkalaphiban, K. et al. Transcriptome-wide investigation of stop codon readthrough in Saccharomyces cerevisiae. *PLOS Genet.* **17**, e1009538 (2021).
104. Wangen J. R., Green R. Stop codon context influences genome-wide stimulation of termination codon readthrough by aminoglycosides. eLife. **9**:e52611 (2020).
105. Loughran, G. et al. Evidence of efficient stop codon readthrough in four mammalian genes. *Nucleic Acids Res.* **42**, 8928–8938 (2014).
106. Fromm, S. A. et al. The translating bacterial ribosome at 1.55 Å resolution generated by cryo-EM imaging services. *Nat. Commun.* **14**, 1095 (2023).
107. Gromadski, K. B. & Rodnina, M. V. Kinetic determinants of high-fidelity tRNA discrimination on the ribosome. *Mol. Cell*. **13**, 191–200 (2004).
108. LaRiviere, F. J., Wolfson, A. D. & Uhlenbeck, O. C. Uniform binding of aminoacyl-tRNAs to elongation factor Tu by thermodynamic compensation. *Science*. **294**, 165–168 (2001).
109. Negrutskii, B. S. & Deutscher, M. P. Channeling of aminoacyl-tRNA for protein synthesis in vivo. *Proc. Natl. Acad. Sci. USA*. **88**, 4991–4995 (1991).
110. Stapulionis, R. & Deutscher, M. P. A channeled tRNA cycle during mammalian protein synthesis. *Proc. Natl. Acad. Sci. USA*. **92**, 7158–7161 (1995).
111. Godinic-Mikulcic, V. et al. Archaeal aminoacyl-tRNA synthetases interact with the ribosome to recycle tRNAs. *Nucleic Acids Res.* **42**, 5191–5201 (2014).
112. Hausmann, S., Ramirez, A., Schneider, S., Schwer, B. & Shuman, S. Biochemical and genetic analysis of RNA cap guanine-N2 methyltransferases from Giardia lamblia and Schizosaccharomyces pombe. *Nucleic Acids Res.* **35**, 1411–1420 (2007).
113. Nguyen T.-T., Stahl G., Déquard-Chablat M., Contamine V., Denmat SH-L. The eukaryotic ribosomal protein S15/uS19 is involved in fungal development and its C-terminal tail contributes to stop codon recognition [Internet]. bioRxiv; 2020 [cited 11 Dec 2022]. pp. 2020.02.09.940346. Available from: https://www.biorxiv.org/content/10.1101/2020.02.09.940346v1
114. Zeeshan, H. M. A., Lee, G. H., Kim, H.-R. & Chae, H.-J. Endoplasmic reticulum stress and associated ROS. *Int. J. Mol. Sci.* **17**, 327 (2016).
115. Yin, S. et al. A murine model of chronic lymphocytic leukemia based on B cell-restricted expression of Sf3b1 mutation and Atm deletion. *Cancer Cell*. **35**, 283–296.e5 (2019).
116. Lazarian, G. et al. A hotspot mutation in transcription factor IKZF3 drives B cell neoplasia via transcriptional dysregulation. *Cancer Cell*. **39**, 380–393.e8 (2021).
117. Morgado-Palacin, L. et al. Partial loss of Rpl11 in adult mice recapitulates diamond-blackfan anemia and promotes lymphomagenesis. *Cell Rep.* **13**, 712–722 (2015).
118. Vitale, I., Galluzzi, L., Castedo, M. & Kroemer, G. Mitotic catastrophe: a mechanism for avoiding genomic instability. *Nat. Rev. Mol. Cell Biol.* **12**, 385–392 (2011).
119. Gujar, V., Li, H., Paull, T. T., Neumann, C. A. & Weyemi, U. Unraveling the nexus: genomic instability and metabolism in cancer. *Cell Rep.* **44**, 115540 (2025).
120. Barlow, J. L. et al. A p53-dependent mechanism underlies macrocytic anemia in a mouse model of human 5q- syndrome. *Nat. Med.* **16**, 59–66 (2010).
121. Montoro, M. J. et al. Influence of TP53 gene mutations and their allelic status in myelodysplastic syndromes with isolated 5q deletion. *Blood*. **144**, 1722–1731 (2024).
122. Schneider, R. K. et al. Rps14 haploinsufficiency causes a block in erythroid differentiation mediated by S100A8 and S100A9. *Nat. Med.* **22**, 288–297 (2016).
123. Yu, L., Yu, T.-T. & Young, K. H. Cross-talk between Myc and p53 in B-cell lymphomas. *Chronic Dis. Transl. Med.* **5**, 139–154 (2019).

124. Campo, E. et al. The 2008 WHO classification of lymphoid neoplasms and beyond: evolving concepts and practical applications. *Blood*. **117**, 5019–5032 (2011).
125. Kowarz, E., Löscher, D. & Marschalek, R. Optimized Sleeping Beauty transposons rapidly generate stable transgenic cell lines. *Biotechnol. J.* **10**, 647–653 (2015).
126. Sanjana, N. E., Shalem, O. & Zhang, F. Improved vectors and genome-wide libraries for CRISPR screening. *Nat. Methods*. **11**, 783–784 (2014).
127. Doench, J. G. et al. Rational design of highly active sgRNAs for CRISPR-Cas9–mediated gene inactivation. *Nat. Biotechnol.* **32**, 1262–1267 (2014).
128. Quijada-Álamo, M. et al. Dissecting the role of TP53 alterations in del(11q) chronic lymphocytic leukemia. *Clin. Transl. Med.* **11**, e304 (2021).
129. McGlincy, N. J. & Ingolia, N. T. Transcriptome-wide measurement of translation by ribosome profiling. *Methods*. **126**, 112–129 (2017).
130. Chothani, S. et al. deltaTE: detection of translationally regulated genes by integrative analysis of Ribo-seq and RNA-seq data. *Curr. Protoc. Mol. Biol.* **129**, e108 (2019).
131. Dobin, A. et al. STAR: ultrafast universal RNA-seq aligner. *Bioinformatics*. **29**, 15–21 (2013).
132. Subramanian, A. et al. Gene set enrichment analysis: a knowledge-based approach for interpreting genome-wide expression profiles. *Proc. Natl. Acad. Sci.* **102**, 15545–15550 (2005).
133. Iyer M. K. et al. The landscape of long noncoding RNAs in the human transcriptome. *Nat. Genet.* **47**: 199–208 (2015).
134. Li H. Aligning sequence reads, clone sequences and assembly contigs with BWA-MEM [Internet]. arXiv; 2013 [cited 19 Dec 2025]. http://arxiv.org/abs/1303.3997
135. Fantini, D., Vidimar, V., Yu, Y., Condello, S. & Meeks, J. J. MutSignatures: an R package for extraction and analysis of cancer mutational signatures. *Sci. Rep.* **10**, 18217 (2020).
136. McKenna, A. et al. The Genome Analysis Toolkit: a MapReduce framework for analyzing next-generation DNA sequencing data. *Genome Res.* **20**, 1297–1303 (2010).
137. Kim S. et al. Strelka2: fast and accurate calling of germline and somatic variants. *Nat. Methods*. 15:591–594 (2018).
138. Ching, T., Huang, S. & Garmire, L. X. Power analysis and sample size estimation for RNA-Seq differential expression. *RNA*. **20**, 1684–1696 (2014).
139. Benjamin D. et al. Calling Somatic SNVs and Indels with Mutect2 [Internet]. bioRxiv; 2019 [cited 19 Dec 2025]. 861054. Available from: https://www.biorxiv.org/content/10.1101/861054v1

Acknowledgements

We are grateful to Nicoletta Cieri, Nira Krasnow, Chip Stewart and Martin Aryee for helpful discussions. We acknowledge Sam Pollock, Lan Nguyen, Fanny Dao, and Candace Patterson for expert project management. We thank the Dana-Farber Flow Cytometry Core, the Broad Institute Walk-Up Sequencing Core, and the Dana-Farber Cancer Institute animal research facility technical team for their technical support. This study was supported by a grant from the National Institutes of Health (NIH)/National Cancer Institute (NCI) (P01 CA206978 and P01-CA081534). CJW is the Lavine Family Chair of Preventative Therapies at Dana-Farber Cancer Institute. C.J.W. acknowledges support from the NIH/NCI (R01 CA216273, U10 CA180861) and from the CLL Global Foundation, and is a member of the Parker Institute for Cancer Immunotherapy at Dana-Farber Cancer Institute, whose work is supported, in part, by the Parker Institute for Cancer Immunotherapy. C.G. is a Scholar through the American Society of Hematology MMSAP Program and the F31 Diversity Individual Predoctoral Fellowship program through the NCI (5F31CA239443-03). M.K. is supported by a Cancer Research UK Clinician Scientist Fellowship (RCCFELCSF-May21\100002). S.L. is supported by the NCI Research Specialist Award (R50CA251956).

Author contributions

C.G. and M.K. designed the murine and cell line models, performed experiments, and analyzed data. C.G., N.R., M.K., P.W., T.O., D.F., S.C., and S.L. participated in library preparation and analysis of RNA-seq, Ribo-seq, proteomics, and WGS data. C.G., M.K., P.W., C.C., B.S., S.S., A.B., A.N., A.L., E.W., N.D., E.T.H., G.B.H., M.J.L., E.W., B.W., L.P., M.H.S., S.Y., A.A. and S.L. performed experiments involving the murine models. F.L., F.G., T.S., J.P., M.Z. and R.C. processed and analyzed immunostaining. G.L., B.A.K., Z.L., and F.C. provided patient samples and clinical data. B.A.K., E.S.L., T.O., and D.F. performed analyses of patient data. A.A., L.W., S.T., K.J.L., D.N., F.C., G.G., A.R., S.C., E.T.H., R.C., S.S., and C.J.W. helped to design and guide the research. D.N. supervised statistical analyses. C.G., N.R., M.K. and C.J.W. wrote the manuscript. All authors discussed and interpreted results.

Competing interests

C.J.W. holds equity in BioNtech, Inc., receives research funding from Pharmacyclics, and is a scientific advisory board member of Repertoire, Adventris, Aethon Therapeutics and Nature's Toolbox, Inc. G.G. receives research funds from IBM and Pharmacyclics and is an inventor of several bioinformatics-related patents, including those related to MuTect and ABSOLUTE. All other authors do not have any relevant conflict of interest.

Additional information

Supplementary information The online version contains supplementary material available at https://doi.org/10.1038/s41467-026-70655-1.

Correspondence and requests for materials should be addressed to Catherine J. Wu.

Peer review information *Nature Communications* thanks Rosa Lapalombella and the other, anonymous, reviewer(s) for their contribution to the peer review of this work. A peer review file is available.

Reprints and permissions information is available at http://www.nature.com/reprints

Publisher's note Springer Nature remains neutral with regard to jurisdictional claims in published maps and institutional affiliations.

Open Access This article is licensed under a Creative Commons Attribution-NonCommercial-NoDerivatives 4.0 International License, which permits any non-commercial use, sharing, distribution and reproduction in any medium or format, as long as you give appropriate credit to the original author(s) and the source, provide a link to the Creative Commons licence, and indicate if you modified the licensed material. You do not have permission under this licence to share adapted material derived from this article or parts of it. The images or other third party material in this article are included in the article's Creative Commons licence, unless indicated otherwise in a credit line to the material. If material is not included in the article's Creative Commons licence and your intended use is not permitted by statutory regulation or exceeds the permitted use, you will need to obtain permission directly from the copyright holder. To view a copy of this licence, visit http://creativecommons.org/licenses/by-nc-nd/4.0/.

© The Author(s) 2026

[1]Harvard Medical School, Boston, MA, USA. [2]Department of Medical Oncology, Dana-Farber Cancer Institute, Boston, MA, USA. [3]Broad Institute of MIT and Harvard, Cambridge, MA, USA. [4]Institute of Cancer and Genomic Sciences, University of Birmingham, Birmingham, UK. [5]Centre for Clinical Haematology, Queen Elizabeth Hospital Birmingham, Birmingham, UK. [6]Northeastern University, Boston, MA, USA. [7]Massachusetts Institute of Technology, Cambridge, MA, USA. [8]Goodman Faculty of Life Sciences, Bar-Ilan University, Ramat Gan, Israel. [9]Department of Pathology, Brigham and Women's Hospital, Boston, MA, USA. [10]INSERM, U978, Université Paris 13, Bobigny, France. [11]Laboratoire d'Hématologie, APHP Hôpital Avicenne, Bobigny, France. [12]Department of Biochemistry and Molecular Biology, Pharmacy School, Universidad Complutense de Madrid, Madrid, Spain. [13]Translational Immunogenetics Lab, Dana-Farber Cancer Institute, Boston, MA, USA. [14]Department of Systems Biology, Beckman Research Institute, City of Hope, Duarte, CA, USA. [15]Department of Data Sciences, Dana-Farber Cancer Institute, Boston, MA, USA. [16]Center for Cancer Research, Massachusetts General Hospital, Boston, MA, USA. [17]Department of Pathology, Massachusetts General Hospital, Boston, MA, USA. [18]These authors contributed equally: Catherine Gutierrez, Marwan Kwok, Neil Ruthen.
✉e-mail: catherine_wu@dfci.harvard.edu